LRP 733/02 October 2002

Papers
Presented at the

**22nd Symposium of Fusion Technology**

Helsinki, Finland
September 2002

available in colour on the web at
crppwww.epfl.ch/conferences

ISSN 0458-5895

LIST OF CONTENTS


| | | Page |
|---|---|---|
| - | DESIGN STUDY OF A TEST STAND FOR ITER GYROTRON<br>*D. Fasel, S. Alberti, T. Bonicelli, R. Cleasen, T. Goodman, J.P. Hogge, A. Perez, M. Santinelli, A. Sterk, M.Q. Tran, T. Verhoeven* | 1 |
| - | UPGRADE OF THE DIAGNOSTIC NEUTRAL BEAM INJECTOR FOR THE TCV TOKAMAK<br>*A.N. Karpushov, G.F. Abdrashitov, I.I. Averboukh, P. Bosshard, I. Condrea, B.P. Duval, A.A. Ivanov, V.V. Kolmogorov, J. Mlynar, A. Perez, I.V. Shikhovtsev, A.N. Shukaev, H. Weisen* | 7 |
| - | PRESENT AND PERSPECTIVE ROLES OF SOFT X-RAY TOMOGRAPHY<br>*J. Mlynar, B.P. Duval, J. Horacek, J.B. Lister* | 13 |
| - | ANALYSIS OF THE MEASUREMENT OF THE CURRENT SHARING TEMPERATURE IN THE ITER TF MODEL COIL<br>*C. Marinucci, L. Bottura, P. Bruzzone* | 23 |
| - | DC BEHAVIOUR OF NbTi CABLE-IN-CONDUIT CONDUCTORS FOR ITER-FEAT<br>*R. Wesche, B. Stepanov, M. Vogel, T. Gloor, P. Bruzzone* | 30 |
| - | DINA SIMULATIONS OF TCV ELECTRON CYCLOTRON HEATING DISCHARGES<br>*V.E. Lukash, D. Raju, V.N. Dokouka, J.-Y. Favez R.R. Khayrutdinov, J.B. Lister* | 37 |

# DESIGN STUDY OF A TEST STAND FOR ITER GYROTRON

D. Fasel[1], S.Alberti[1], T.Bonicelli[2], R.Cleasen[3], T.Goodman[1], J.P. Hogge[1], A. Perez[1], M. Santinelli[3], A. Sterk[4], M.Q. Tran[1], T. Verhoeven[4]

[1]Centre de Recherches en Physique des Plasmas
Association EURATOM-Confédération Suisse, EPFL, CH-1015 Lausanne / Switzerland
[2]EFDA-CSU, Max Planck Institut, Bolzmannstr. 2, D-85748 Garching / Germany
[3]ENEA, Via E. Fermi 45, I-00044 Frascati (Roma) / Italy
[4]FOM-Institute for Plasma Phyiscs "Rijnhuizen", P.O.Box 1207, NL 3430 BE

**ABSTRACT**

In the frame of development of the ITER electron cyclotron wave (ECW) system, the development of a 170 GHz, 2 MW CW coaxial gyrotron with depressed collector is foreseen in the European Technology Workplan, during the 6th Framework Program (2003-2006). Such development relies on the availability of a test stand capable of providing the electrical energy and cooling capacity. This test stand will possibly be used, in a later stage, for the component test of the ITER ECW system.
This paper will first presents the main parameters of this new coaxial gyrotron. Then we describe the test stand itself, including the general requirements for testing and evaluating the behaviour of the RF source. Then follows a description of the electrical system design. Compared to the ITER reference design, the test stand emphasises the requirement of flexibility, which is necessary during the development of the gyrotron. The additional electrical equipment, such as the body power supply or the series solid-state switch, is included in the overview of the electrical system.
The cooling system will be an important part of the design study. Indeed, the design efficiency of such depressed collector gyrotron is ~50%, implying that more than 4 MW of continuous heat dissipation and evacuation by the cooling equipment. The specifications of the cooling system must also comply with ITER reference design values.

## 1. BACKGROUND

High power electromagnetic waves at the electron cyclotron frequency will be used on ITER-FEAT for heating, current drive and MHD control. It is foreseen to inject 20 MW-CW at 170 GHz using gyrotrons as electromagnetic wave sources. In the reference design, a 1 MW-CW gyrotron is foreseen with a total of 24 units. It is widely recognised, however, that higher unit power (~ 2 MW/gyrotron) is highly desirable since such a tube would strongly reduce the total cost and result in a simpler system.
The European fusion program has been developing a 2 MW coaxial gyrotron for many years. The short pulse results indicate that such a tube configuration can achieve power level in excess of 2 MW. High power windows of the new diamond generation can be produced, which handle 2 MW-CW power.
In view of the interesting capabilities of coaxial gyrotrons as high power (2 MW) CW sources, EFDA has decided to start a design study of an industrial 2 MW-CW coaxial gyrotron. This study will include contributions from three European Associations (CRPP, FZK and TEKES) and industry. The association will perform calculations to define the main elements of the tube such as the electron gun, the cavity, the quasi-optical mode converter etc., whilst taking into account technological constraints defined by industry, who determine the main operating parameters such as, the rated currents and voltages, the flow rate and I/O pressures of the cooling circuit. The target values are summarised in the Table 1.

## 2. GENERAL CONSIDERATIONS

As mentioned above, the CW 2MW coaxial gyrotron, proposed by EU as a new RF source for ITER, is still in its initial stage. In the near future (2004-2005), the associations in charge of the project will require a test facility, outside the industrial environment, to validate the target gyrotron parameters, like: RF output power measurement, mode purity, short pulse to CW working mode, thermal stability of the cavity etc. In addition, over a longer period of time, several gyrotrons (at least 12) will be commissioned before installation and use on ITER. A test bed would clearly be more appropriate for commissioning the RF sources, than the ITER environment that must comply

with other criteria: short installation period, limited number of measurements, fixed working scenario, etc.
In the following chapters, we will present the most important characteristics of the test facility components we expect, for the development and testing and compliance with ITER.

| | |
|---|---|
| **RF frequency** | 170 GHz |
| **Nominal RF Power** | 2 MW |
| **Nominal pulse length:** | CW |
| **Depressed collector:** | Yes |
| **Diamond window** | Yes |
| **RF output efficiency:** | ≥45% |
| **Body to collector capacitance** | ~2.5 nF |
| **Main power supply (Collector to cathode):** | |
| ▪ **Voltage** | <60kV/ |
| ▪ **Current** | 90A |
| **Body power supply:** | |
| ▪ **Voltage** | 30 kV |
| ▪ **Current (steady state)** | 0.2A |

**TABLE 1: Design parameters of the 2MW coaxial gyrotron**

## 3. ELECTRICAL SUPPLY STRUCTURE

All power will be drawn from the grid. So, for a gyrotron efficiency >45 % (see Table 1), the delivered active power will be at least 4.5MW. The reactive power consumed by the main power supply itself must also be included. In the worst case, depending on the structure considered, the apparent power demand is not expected to exceed 6MVA.
The grid supplying the test facility must also fulfill the following requirements:

- The capability to continuously deliver power, as well as short pulses (1-100 msec) in the initial phases. ie. the short circuit impedance of the source must be sufficient to avoid disturbances reflected on other users, and to respect the standards defined in the EN 50160 norm.
- Both the prototype development and tests as commissioning are little or not compatible with perturbed power lines or with long supply interruption periods (> 1 week).

### 3.1 THE MAIN POWER SUPPLY

The ITER reference design (see [1]) is based on diodes power supplies, connected in series, on the DC side, with thyristor bridges in order to adapt the level of the output DC voltage, if needed. A simple and robust control system such as HVPS should be contrasted with the need to account for the relatively slow output voltage variation and the large amount of energy stored in the passive filtering components used to damp the inherent ripple of such design and the higher reactive power consumption. Thus, within the frame of a test stand, we have the opportunity to transform these disadvantages, with a PSM like design (see [2]), which is already in use in the additional heating of TCV for few years (see [4]). Such an installation is also under construction for the ECRH on W7X. Such a design does not require additional components to ensure a fast switch off in the case of a

fault in the gyrotron (arcs or other events). The DC voltage output modulation is also intrinsically available, up to 10 kHz.

### 3.2 THE BODY POWER SUPPLY

To increase the total efficiency of the gyrotron, the present proposal is based on the positive polarisation (30-40 kV) of the anode cavity and of the quasi-optical converter (body), such that the spent beam is decelerated before reaching the collector as referred to ground.
The **B**ody **P**ower **S**upply (BPS) is used to apply a potential on the body, in order to reach a final maximum acceleration beam voltage of 90kV.
The particularity of the coaxial gyrotron, is the coaxial design of its cavity, which significantly lowers the ohmic losses, with a power density on the coaxial insert < 100W/cm2. This coaxial design, however, dramatically increases the capacitance between body and collector. A typical value for a gyrotron capacitance is between 200 and 300 pF, whereas the capacitance between body and ground of the first coaxial prototype was found to be 2.5 nF. The equivalent design studied for the ECRH system in the framework program of JET-EP [3] was not longer appropriate with this value.
A development program leading to the manufacturing and testing a BPS prototype [4] for the coaxial gyrotron has been launched. A concept and feasibility study was undertaken accounting for the expected ITER requirements. The specifications in Table 2 were assumed for the BPS, for a fully solid state design. Indeed, beside being energy efficient, it is also expected to yield considerable advantages in term of procurement costs, operation and maintenance requirements, compared to more traditional vacuum based solutions.

| | |
|---|---|
| **Body to Cathode voltage** | 90kV [1] |
| **Body to Collector voltage** | 45kV [1] |
| **Modulation depth** | 25kVpp [2] |
| **DC Accuracy** | ±0.5% |
| **Output ripple** | ±1.0% |
| **Bandwidth (sinus, -3dB)** | DC - 10kHz |
| **Ramp up time** | ≤ 65µs |
| **Switch-on maximum overshoot** | ±1%, ±900V [3] |
| **Switch-on max. settling time** | 50 µs |
| **Switch-off time** | < 10 µs |
| **Maximum energy delivered to the load in case of an arc** | 10J |
| **Duty Cycle** | CW |

[1] Maximum value
[2] Peak-peak value from 20kV to 45kV
[3] This value is specified on the total acceleration voltage: 90 kV

**TABLE 2 – Main BPS Specifications**

Two supply schemes are possible: the BPS potential is referred to the cathode, so in this case the voltage is applied between cathode and body; the BPS is referred to ground potential. The second possibility is favoured for the following reasons:

- a lower insulation level, which has a large impact for a fully solid state design
- a lower voltage slew rate during the transients
- no floating potential (a great advantage for the control electronics)
- a reasonable cost reduction.

In revenge, all fluctuations appearing on the main voltage (Vk) must be compensated by an accurately regulated output voltage of the BPS. That requires two voltage dividers, measuring the

Vk and Vb potentials, matched together with sufficient bandwidth and accuracy, to ensure the RF power control in the required range. Assuming this choice, a peak current of approximately 3A, due to a high capacitance value (see Table 1), must be drawn during transients, which significant compared to the specified DC current (200 mA). The study investigates a few possible designs able to achieve these parameters listed in the Table 2. A PSM like principle was finally identified as the best compromise (see [3]).
The main difficulty of this topology is to make available many insulated DC sources via a multi-secondary transformer and the complexity of cabling and connections. Indeed, although the power design value of this transformer is rather low (~70 kVA as peak power), the overall size and the weight are relatively large (1800x650x1800mm, 1600kg). Another problem, inherent in this design remains unsolved: the short-circuit detection of one secondary among the others. These weaknesses will be addressed during the prototype design phase. The BPS will be integrated in the test stand structure. Thus, the control interface, including the warning and protections signals, the measurements, the working status, will also be addressed during this next phase. Particular attention will be paid to operational safety of the complete installation: as example, the synchronisation between the main HVPS and the BPS during the startup and shutdown phase, or during the HVSS modulation phase as described below.

### 3.2 THE SERIES SWITCH (HVSS)

When using a main HVPS capable of only slow voltage output slew rate, an additional device to ensure a fast switch off in case of fault is required ( mainly arcs inside the beam tunnel). Energy deposition must be limited to <10 Joules (see Table 1). A fast solid-state switch will be connected in series with the gyrotron to achieve this goal, which can disconnect the gyrotron from the power supply within a few microseconds. Should the IGBT switch fail to switch-off, a crowbar will be triggered to short-circuit the output of the power supply.

The specifications for this HVSS are listed in Table 3. These requirements are already partially fulfilled by existing devices on the market [4]. Only modulation capability will require further improvements. Using only the body voltage as control on the RF could result in an excessive overheating of the collector (see [5]). Controlling the RF power with the HVSS would significantly reduce the average collector loading.

| | |
|---|---|
| **Rated load voltage** | 50 kV |
| **Maximum voltage** | 80 kV |
| **Rated continuous current** | 90 A |
| | |
| **Breaking current:** | 1 kA |
| **Breaking time:** | < 5μs |
| **Operation frequency** | Up to 5 kHz |

**TABLE 3: Electrical Design parameters for the HVSS**

In EU, several contacts with industrial partners have been launched. The proposal from ABB semiconductors appears to be the more promising. An IGBT stack, usually working as a fast crowbar in industrial processes or, as part of the design for the HVDC power station, is foreseen. In our case, a prototype should demonstrate that the increased power demand of the IGBT driving electronics during fast modulation can be fulfilled without major changes to the existing design.

## 4. THE COOLING SYSTEM

Considering that some hundreds of kW are required for auxiliaries in addition to the electrical power needs for the gyrotron itself, a total heat load of 5 MW has to be evacuated. Present day gyrotron installations have such duty cycles, that most of the components can make use of their thermal inertia. For continuous operation, the heat generation and evacuation studies do not permit this approach.

### 4.1 THE PRIMARY CIRCUIT

Water remains the most common cooling fluid due to its heat transfer capability. Depending on the site requirements, the delta T allowed in the primary circuit water will determine the flow rate required to evacuate the dissipation heat: eg: a delta T of 10 deg would impose a flow rate >120 litres/sec.
The input water temperature will also have an impact on the heat exchanger size. As the maximum water temperature is imposed at the output of the gyrotron (collector, window, mirrors), if the input temperature of the primary circuit is increased, the operational temperature range of the heat exchanger decreases, increasing the necessary exchanger volume.
Finally, fluctuations on the input water temperature could influence the RF power measurements in the dummy load, or at least, increases the complexity and cost of this installation.

### 4.2 THE SECONDARY CIRCUIT

The secondary circuits are dependant on the gyrotron design. As the prototype is not yet manufactured, estimations have been made on the requirements of an existing 1 MW gyrotron [5]. Two classes of circuitry are identified:

- A "high" pressure circuit (4 to10 bars), ensuring the cooling of the cavity and of the mirrors (~200litres/min)
- A "low" pressure circuit (1 to 2 bars) to evacuate the heat losses of the collector (40 litres/sec).

A volume of clean and/or deionised water must be maintained available for a reasonable cost.

## 5. THE CONTROL AND ACQUISITION SYSTEM

In the particular case of a test stand, the control and acquisition system is an important part of the evaluation, because the main purpose of the installation is to obtain as much information as possible about the behaviour of the tested device.

The prototype often includes much more controlling signal than for a production gyrotron. These signals must be configured for real-time comparison with control signal, for test scenarios and operational warning levels to interrupt the sequence when danger conditions are detected.

For a gyrotron, it is usual to control the currents, the voltages, the vacuum and the auxiliaries, such as the cooling system and cryogenic temperatures. In addition, a prototype will need:

- Several temperatures probes (10 to 20) placed around the cavity (collector) to verify the thermal design and to detect hot points.
- The water flow and temperatures in the cooling circuits (cavity, collector, window), to allow for losses estimations.
- The behaviour of the diamond window

The acquisition must comply with two requirements, relevant to the working period of this future gyrotron: from only msec to CW.

Data must be available to the operators, for a short acquisition period, with a high sampling period (at least 1 Ms/sec). This type of acquisition will be triggered exclusively on events, for use in the analysis of undesirable transients during a pulse.

The data will also be recorded at a lower sampling period, but continuously during the entire shot, to characterise the gyrotron evolution, with repeated shots, and to certify the design operation.

## 6. FUTURE EXTENSION AND CONCLUSION

The test stand may be used, in a future extension, to test RF delivery from gyrotrons to the ITER port. This would imply:

- Installing the RF waveguide as defined for ITER, with the specific vacuum auxiliaries
- Integrating parts of an ITER launcher prototype in the test stand installation: mirrors, mechanical structure, vacuum auxiliaries.

To conclude, a preliminary study has been made by the CRPP to define the characteristics of a test stand. Both the technical parameters and the engineering of the project could be performed by our laboratory. A budgetary estimate has been performed. The next step should involve a detailed specification taking into account the choices of different components described in this paper, and integrating all of them in a final test stand study.

## REFERENCES

[1] DDD4.1 (Design Description Document of ITER) :"Pulsed Power Supplies"

[2] D.Fasel and al., "Design and operation of...", SOFT 1996, vol.1, p.569-572

[3] T.Bonicelli, R Claesen, A Coletti, PL Mondino, M Pretelli, M Santinelli, G Taddia: "High Frequency/High Voltage Solid State Body Power Supplies for CPD Gyrotrons", to be presented at 22nd SOFT, Helsinki, September 2002

[4] A.B.Sterk, A.G.A. Verhoeven, the ECRH team: "Design and R&D for an ECRH power supply and power modulation system on jet", to be presented at 22nd SOFT, Helsinki, September 2002

[5] G.Dammertz and al., "Power modulation capabilities of the 140GHz/1MW gyrotron for the stellarator W7-X", to be presented at 22nd SOFT, Helsinki, September 2002

# Upgrade of the Diagnostic Neutral Beam Injector for the TCV Tokamak

A.N.Karpushov[1], G.F.Abdrashitov[2], I.I.Averboukh[2], P.Bosshard[1], I.Condrea[1], B.P.Duval[1], A.A.Ivanov[2], V.V.Kolmogorov[2], J.Mlynar[1], A.Perez[1], I.V.Shikhovtsev[2], A.N.Shukaev[2], H.Weisen[1]

[1] *Centre de Recherches en Physique des Plasmas, Association EURATOM – Confédération Suisse, EPFL, 1015 Lausanne, Switzerland*

[2] *Budker Institute of Nuclear Physics, 630090, Novosibirsk, Russia*

## Abstract

The paper summarizes the technical and experimental efforts on Diagnostic Neutral Beam Injector (DNBI) [1,2] application on the TCV (Tokamak à Configuration Variable) [3-5]. The main task of the DNBI is to provide together with Charge eXchange Recombination Spectroscopy (CXRS) [2] a local measurement of plasma ion temperature, velocity and impurity density. A series of DNBI technical upgrades was undertaken to increase the neutral beam current density in the observation region, which was required to extend the operational range of the CXRS diagnostic. The aim of DNBI upgrade, presented in this paper, is to increase the full energy beam current density in plasma by a factor of 2. A new ion source was installed on DNBI with corresponding changes in power supplies. The diameter of RF cylindrical plasma box and the extraction area of ion optical system were also increased; the full energy (52 keV) beam fraction was increased from 0.5 to 1 A.

## 1 Experimental setup of the CXRS and DNBI on the TCV

The diagnostic neutral beam injector (DNBI), manufactured by the Budker Institute of Nuclear Physics (BINP) Novosibirsk, was commissioned at the TCV Tokamak in 2000. It provides, together with the CXRS, a diagnostic tool for a local measurement of the plasma ion temperature from the impurity (carbon) line Doppler broadening [2,6]. The experimental setup of the CXRS is shown in Fig.1. A diagnostic camera head with mirrors was installed inside the vacuum chamber, close to the plasma, observing the full (~60 cm) DNB path in the plasma. Spatial resolution, determined by the viewing chords-flux surfaces intersection at the beam position, is 1.5-3 cm. The C/X light from the beam is focused onto 16 optical fibres, which are connected to a Czerny-Turner spectrometer. The spectra are imaged onto a 2D detector equipped with a front-illuminated EEV CCD, with minimal readout time of 10 ms. The system is designed to observe CX transitions in the visible spectrum, the carbon CVI (n=8→7) transition at λ=5291 Å was used because of the relatively high concentration of carbon (~3%) in plasma. The utilisation of the diagnostic neutral beam allows non-perturbative measurements of plasma ion parameters, but implies low active CX signal intensities compared with heating NB based CXRS diagnostics. The low active to passive signal ratio (A/P~25% for an average plasma density ($n_e$) of $1–2\times10^{19}$ $m^{-3}$ and A/P~5% for $5\times10^{19}$ $m^{-3}$) together with the poor photon statistics limit the performance of the CXRS diagnostic on TCV. Both the CXRS optical system and the DNBI were upgraded to optimise CXRS measurements in high density plasmas ($n_e \geq 6\times10^{19}$ $m^{-3}$). In particular the S/N

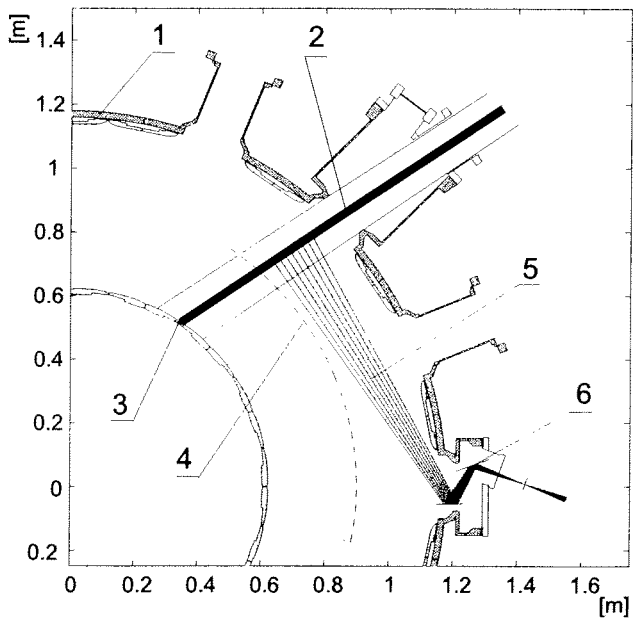


Figure 1: Experimental setup of the CXRS at TCV in horizontal cross-section of the TCV. 1 – TCV vacuum vessel; 2 – beam axis; 3 – thermocouple array at the TCV inner wall; 4 – plasma axis; 5 – CXRS view lines for low-field plasma side; 6 – CXRS diagnostic head.

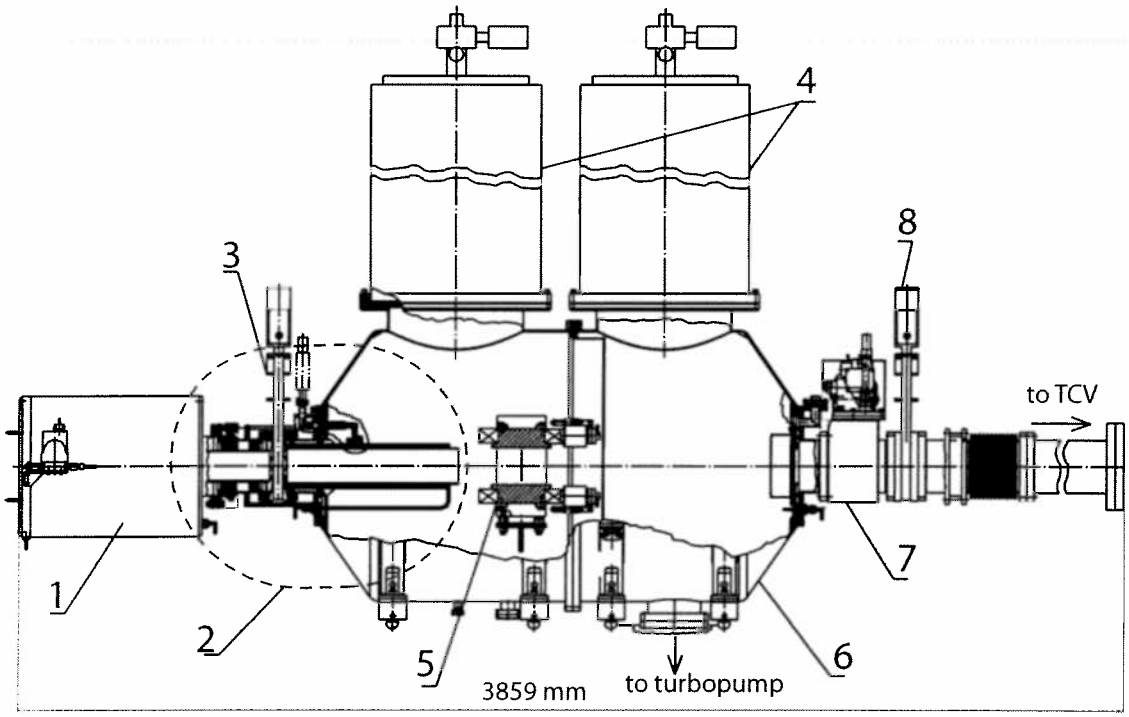


Figure 2: Diagnostic neutral beam injector for TCV
1 – Ion source, 2 – neutraliser; 3 – ion source gate valve; 4 – cryopumpes; 5 – magnetic separator with diaphragm; 6 – vacuum vessel; 7 – movable calorimeter; 8 – TCV gate valve.

ratio was increased by a factor of ~5 by enhancing the spectroscopic system throughput [6] (Fig.5 (A,B)).

## 2 DNBI characteristics

The charge-exchange cross-section for the carbon is optimal for a 50 keV hydrogen beam. The DNBI (Fig.2) (similar to [7]) was designed for the operational energy range 20-55 keV (according the CXRS requirements), an equivalent beam current of the full energy component was of 0.5 A at 50 keV within a 10 cm diameter at the beam focus. The beam is injected at a toroidal angle of $11.25^{O}$ in the horizontal mid-plane. The beam dimensions and alignment were verified inside the TCV vessel by an array of thermocouples on the central column facing the DNB entrance port. The neutral particle density of beam fractions delivered to the plasma (calculated from the relative intensities of the Doppler-shifted $H_{\alpha}$ lines) with full, 1/2, 1/3 and ~1/18 energies was 40:35:20:5 % respectively. The plasma in DNBI source is produced in the RF driven plasma generator (Fig.3). The plasma source is powered by ~5 kW, 4.55 MHz RF generator. The source support systems include water cooling, hydrogen gas supply, gas puff control and a plasma ignition system. Ions are extracted from the cylindrical RF plasma box and accelerated by a four molybdenium grids with an optimal angular spread of the beam, and then neutralised by charge exchange in the gas flow from the plasma source. The first (plasma) and the second (extracting) grids are power supplied by a high voltage modulator (max. 55 kV, 3.7 A), the third (accelerating) grid is

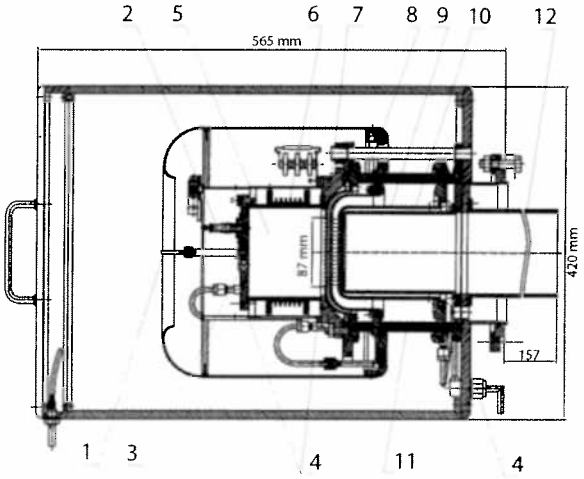


Figure 3: RF ion source.
1 – gas puffing; 2 – ignition; 3 – permanent magnets; 4 – water cooling; 5 – plasma chamber; 6 – RF antenna; 7 – plasma grid; 8 – extracting grid; 9 – accelerating grid; 10 – grounded grid; 11 –isolator; 12 – neutralizer.

biased at -450 V and the fourth (suppressing) grid is grounded. The grids are spherical with a ~4 m radius, to focus at the TCV plasma centre. The neutralisation efficiency of the full energy fraction is about 50%. The neutral beam passes through a vacuum tank and into the TCV beam line. This tank uses a bending magnet, to separate the residual ions from the neutral beam particle, and an insertable segmented calorimeter, used to measurement of the beam profile. Two liquid He cryopumps, each with a pumping speed of 24 $m^3s^{-1}$, limit the pressure at the beam duct $<10^{-3}$ Pa during operation.

A new ion source with corresponding changes in power supplies was installed in the frame of the DNBI technical upgrades. The diameter of RF cylindrical plasma box was increased from 10 to 12 cm, the extraction area was increased from 72 to 92 mm and the number of cylindrical apertures in the grids was increased from 163 to 241. The full energy (52 keV) beam fraction was increased from 0.5 to >1 A and the total extracted ion current – from 1.65 to 2.7 A. Optimisation of the source RF plasma discharge resulted in a full energy fraction delivered to the plasma of >50%. The parameters of the beam before and after upgrade are listed in Table.1.

Table.1 DNBI parameters

| Parameter | Before upgrades (1999) | After upgrades (2002) |
|---|---|---|
| Beam energy ($E_0$) | 20-50 keV | up to 53 keV |
| Beam species | hydrogen or deuterium | hydrogen |
| Ion beam current | 1.65 A | 2.7 A |
| Full energy equivalent current | ~0.5 A | ≥ I A |
| Neutral beam species ($E_0$:$E_0/2$:$E_0/3$:$E_0/18$) (density) | 40:35:20:5% | 52:17:26:5%<br>56:17:23:4% [1] |
| Beam divergence | 0.6-0.7° | ~0.7° |
| Maximum overall pulse duration | 2 s | 1.8 s |
| Beam ON-time range | 1 ms – 2 s | 10 – 150 ms [2] |
| Minimal beam OFF-time | 2 ms | ≥1.5 of ON-time |
| Rise/fall time (10-90%) | <0.2 ms | 2.5/0.25 ms |
| The shortest time between beam pulses | 300 s | |
| Pressure at the exit during operation | $< 10^{-5}$ mbar | |

[1] – for 0.2 ms DNBI pulse
[2] – optimised for 50 ms

One of the fundamental principles of the TCV control system (TCVCS) is the full integration of diagnostics control and acquisition. However, in order to accomplish independent DNBI tests and commissioning, the injector was also equipped with CAMAC hardware, which was controlled by a local PC. A Java routine establishes communication between the DNBI control software and the VMS/Alpha TCV control system. The DNBI timing is controlled by CAMAC times, with the timing and other beam parameters pre-set by the DNBI control software with values from TCV. Once the DNBI sequence is triggered, the CAMAC modules perform the requested sequence. The shot trigger itself may come either from the software control system or externally from TCVCS during plasma operation.

## 3 CXRS measurements and DNB parameters

### *3.1 Beam characteristics.*

A code package was developed to calculate the beam profile and attenuation in the TCV plasma [8]. This is able to determine the 3D intensity of each beam fraction at any point along the beam and at any time in the TCV discharge. The beam attenuation can reach 80% at high density, verified by thermocouple measurements on the TCV central column.

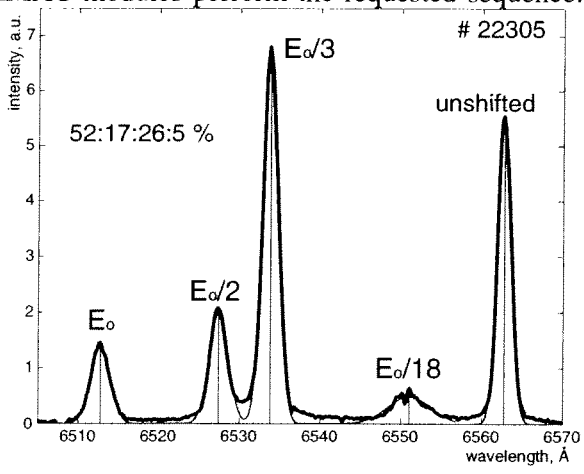


Figure 4: $H_\alpha$ emission: fundamental and three doppler-shifted DNBI components.

The beam current and extraction voltage were measured in the DNBI HV power supply system. Data from an optical doppler-shifted $H_\alpha$ emission measurement are used as a monitor of the beam fraction optimisation (Fig.4), and used to deduce the beam fraction components listed in Table 1.

### *3.2 CXRS ion temperature measurements*

The CXRS $T_i$ measurements on TCV were used for study the following physics phenomena [6]: dependence of the energy confinement on the plasma shape and plasma behaviour in presence of additional ECR heating, especially for advanced scenarios with ITB creation by off-axis heating. The DNBI and CXRS system upgrades allow to measure the ion temperature profile for average plasma density up to $6\times10^{19}m^{-3}$ with an Active/Passive ratio ≥20%. The CX carbon VI 5291Å line broadening before and after DNBI and CX detection system upgrades are shown in Fig.5. The CX line intensity for ohmic discharges with different plasma densities are shown in Fig.6. The Active/Passive signal ratio reaches 80 % for TCV ohmic discharges with low ($\sim10^{19}m^{-3}$) density (Fig.6(C)).

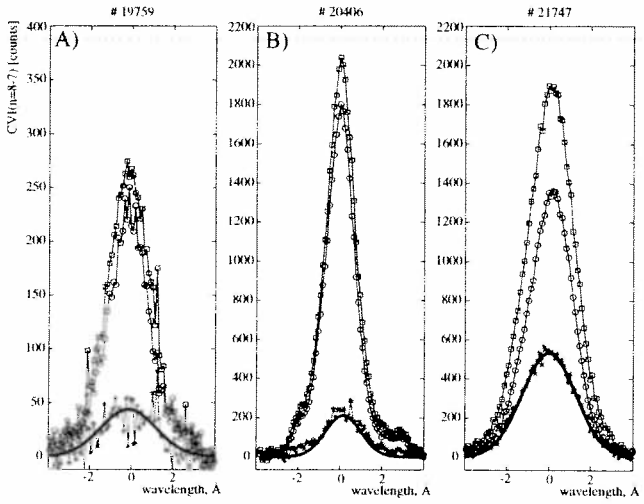


Figure 5 CX CVI lines @5291Å spectrum broadening:
A) before CXRS and DNBI upgrades, $<n_e>=3\times10^{19}m^{-3}$;
B) after CXRS upgrade, $<n_e>=6\times10^{19}m^{-3}$;
C) after CXRS and DNBI upgrades, $<n_e>=6\times10^{19}m^{-3}$,
passive (circles points), active (stars), their sum (squares) and active spectra filling (line).

## 4 Effect of the DNB deposited particles

As mentioned in Section 1, the Active/Passive ratio linearly increases with DNBI current in the observation region. Conversely, the TCV tokamak experimental programme investigates plasma shape effects on plasma confinement in ohmic, ECH and ECCD regimes. TCV does not use additional ion heating system so there is a limit on the maximum injected power without affecting the ion temperature itself. The DNBI-plasma interaction was studied with a Neutral Particle Analyser (NPA). Its high-energy channels (sensitive to the neutrals with energy 3-8~keV escaping plasma) registered an increasing of the CX flux that was correlated with DNBI operation. An experimental and theoretical analysis was performed [9] showing that the increase of the high energy tail of CX neutral flux during DNB injection was caused by CX of fast hydrogen ion population produced as a result DNB deposition in plasma. The experimental results of the DNBI deposited particles relaxation allow us to conclude that:

- For TCV ohmic TCV discharges, 70-90% of the DNB absorbed power is deposited on the electrons so the plasma ion power from the DNB is only 5-15% of that from the plasma electrons (Fig.7).
- The "NPA CX spectrum" during DNB ON and OFF injection phases shows, that the energy transfer from the DNBI deposited ions to plasma ions increases

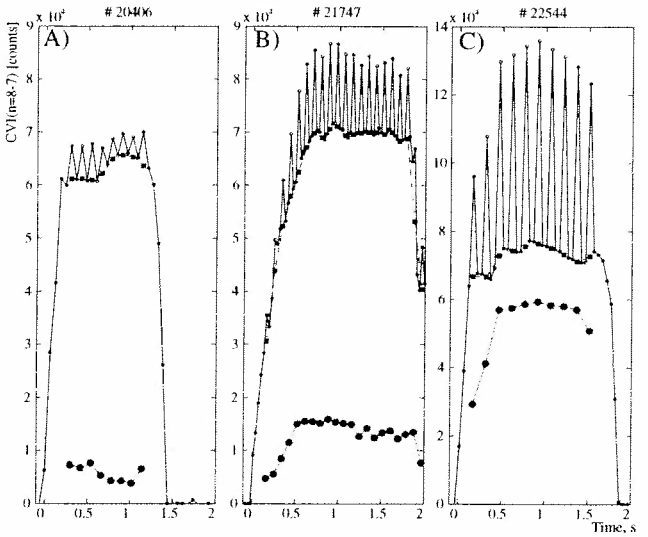


Figure 6: CX CVI lines @5291Å intensity (solid lines) for TCV ohmic shots:
A) before DNBI upgrade, $<n_e>=6\times10^{19}m^{-3}$;
B) after CXRS and DNBI upgrades, $<n_e>=6\times10^{19}m^{-3}$;
C) after CXRS and DNBI upgrades, $<n_e>=2\times10^{19}m^{-3}$, high elongated plasma; active signals (circles points) and extrapolation of the passive signals (squares)

the NPA ion temperature by only 2-10% [9], which is regarded as negligible.

## 5 Conclusion and discussion

A series of DNBI technical upgrades has extended the operational range of the CXRS diagnostic (for electron density up to 6-8×$10^{19}$$m^{-3}$). The full energy beam current density in plasma was increase by a factor of 2, and the beam fraction ratio was also improved. The DNBI is fully integrated in the TCV diagnostic system and provides (in combination with CXRS) the ion temperature measurements for all TCV discharges. The availability of the DNBI reached ~80% of the TCV shots, with a reliability ~90%. CXRS $T_i$ data are available for ~250 TCV shots following the definitive DNBI upgrade in 2002.

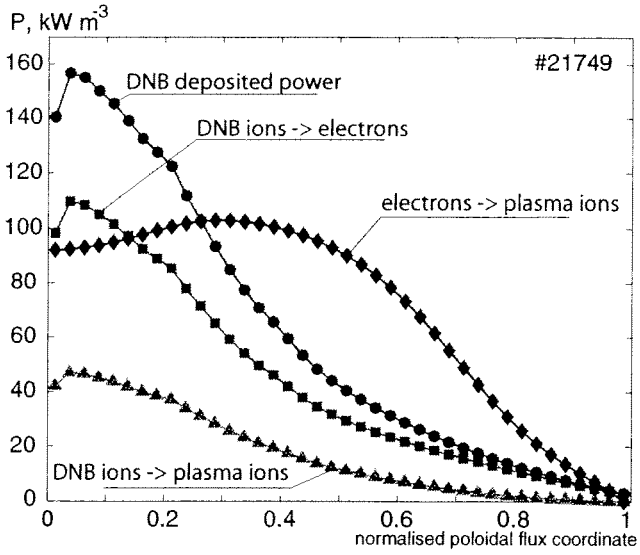


Figure 7: Local ion power balance in TCV ohmic shot with DNB injection.

Further increase of the active to passive signal ratio of the CXRS measurements and extension the operational range up to $n_e \geq 10^{20}m^{-3}$ (X3 ECH) requires an increase of the full energy fraction beam current density in the observation region without further increasing the injected power. In this situation we are considering the following improvements in the DNBI performance:

- The replacement of the RF DNBI plasma source by an arc source: This would provide an increase the density of the full energy beam fraction from ~50% to ~80%. There are however problems with source lifetime.
- The reducing the distance from beam source to plasma, the neutral density in TCV could thus be increased by a factor of 1.2-1.3;
- Changing of the beam shape: The usable beam density could be increased by making the beam elliptical. This can be achieved without increasing the total injected neutral power. A source grid with slits instead of the current arrangement of holes is being considered.
- Further improvements in the optical CXRS system would permit statistically valid data with shorter integration times which would directly improve the passive radiation subtraction quality, permitting measurements in plasma discharges with fast changing parameters.

## Acknowledgements

The authors appreciate the support of the both the TCV and BINP technical, engineering and scientific stuff, which participate in development, manufacturing, installation and upgrade of the DNBI on TCV.

This work was partly supported by the Swiss National Science Foundation.

## References

1. J.Mlynar et al., Diagnostic Neutral Beam injector at the TCV Tokamak, CRPP report LRP 710/01, CRPP-EPFL, Lausanne, 2001.
2. P.Bosshard, B.P.Duval, J.Mlynar, H.Weisen, 28th EPS Conf. on Contr. Fusion and Plasma Phys., Madera, Portugal, ECA Vol. 25A, (2001), 365-368.
3. F Hofmann et al., Plasma Phys. Control. Fusion, 36 (1994) B277-B287
4. F Hofmann et al., Plasma Phys. Control. Fusion, 43 (2001) A161–A173.
5. J.-M. Moret, ECH physics and new operational regimes on TCV, Plasma Phys. Control. Fusion (to be published in 2002).
6. P.Bosshard, B. P. Duval, A. Karpushov, J. Mlynar, 29th EPS Conference on Plasma Phys. and Contr. Fusion, Montreux, ECA Vol. 26B (2002), P-4.120.

7. A. A. Ivanov et al., Rev. Sci. Instrum., 71 (2002) 3728-3735.
8. J.Mlynar, TCV DNBI Profile and Attenuation Studies with Code Manual, CRPP report LRP 692/01, CRPP-EPFL, Lausanne, 2001.
9. A. Karpushov, P.Bosshard, B. P. Duval, J. Mlynar, 29th EPS Conference on Plasma Phys. and Contr. Fusion, Montreux, ECA 26B (2002) P-4.119.

# Present and perspective roles of soft X-ray tomography in tokamak plasma position measurements

J. Mlynar, B.P. Duval, J. Horacek and J.B. Lister

Centre de Recherches en Physique des Plasmas, Association EURATOM-Confédération Suisse, EPFL, 1015 Lausanne, Switzerland

**Abstract**

This paper shows the importance and feasibility of real-time tomography in fusion experiments for the example of soft X-ray (SXR) position measurements. The requirement of non-magnetic real-time diagnostics in low frequencies for ITER is discussed. This is illustrated by recent results of rapid tomographic inversion of SXR measurements on tokamak TCV. Comparison with the magnetic reconstruction data has not only shown the valuable resolution capabilities of both techniques but also revealed a slight dependence of magnetic measurements on toroidal magnetic field and an unnoticed drift of plasma position observer. A feasibility study using current hardware capacities for programmable real-time tomographic system with plasma position feedback output was carried out. A compact solution is found to be tractable opening wide perspectives for development.

## 1. Introduction, ITER relevance

The computerised tomography technique, which allows the reconstruction of the emissivity cross-section from its line integral measurements, has been applied in fusion plasma science since early 1980's. A review of plasma tomography methods is presented e.g. in [1]. In the past two decades, plasma tomography applications have profited from the computer speed and capacity increase so that quite sophisticated algorithms, with a numerically rigorous introduction of constraints, have been developed. However, one can also retain simpler algorithms for use in tasks with a reduced time window. At JET, this principle was adopted in a real-time transputer tomography system [2] that, however, required significant hardware complexity. At the TCV tokamak [3], we have recently introduced a rapid soft X-ray (SXR) tomography algorithm [4] which enables post-shot plasma position verification and mode activity retrieval. As presented in the following section, the first applications of the fast routine show it to be potentially attractive for TCV

real-time control. In section three, the technical feasibility of this possibility in conjunction with present day hardware systems is discussed.

To meet the stringent requirements on plasma shape control, the ITER feedback control requires accurate diagnostic information. Considerable attention has been given to high frequency problems during the conception of the ITER plasma shape and positional control system that has, to date, been based on magnetic diagnostic information [5].

The long pulse operation of ITER creates new challenges at lower frequencies, with a pulse duration of ~1000s. Since the magnetic fields and fluxes are obtained by electronic integration of sensor voltages, which are themselves proportional to the rate of change of the included magnetic flux, the problem of integrator drift must be addressed. Considerable effort has gone into reducing the drift of the integrator itself, so that reliable operation up to over 3000s is considered reasonable. However, in the neutron flux of ITER the radiation induced electromotive force in the cable mineral insulator dielectric becomes a problem. An alternative measurements of the plasma shape at the lowest frequencies would thus be useful, to verify or correct the potential disturbances in the magnetic measurements.

Combining information from different diagnostics in the sh ape and position feedback control system is not a problem. The power supplies are already separated into fast (for vertical position stabilisation) and slow (for shape control) although the poloidal field coils are common to these separate loops. Diagnostic information can be combined using cross-over filters to give a constant gain and continuous phase. Low-frequency position information, can be similarly merged with high frequency magnetic, compensating for drift in the magnetic system. It would not be feasible to compensate all the magnetic sensors with alternative non-magnetic information. Feedback loops do not require information from all sensors, but only on specific combinations, referred to as the control parameters; such as the current centroid position, the gaps between the separatrix and the walls, and the divertor strike points.

The issue is therefore to provide low-frequency diagnostic information of particular quantities, which can be combined into the estimators of the control parameters. The low-frequency requirement opens the possibility of using diagnostic information extracted from computationally intensive techniques, with measurement estimates made say every 100 seconds with a response delay of up to 5 seconds. The possibilities are numerous and may encompass the real-time tomographic inversion of X-rays emission, visible light or

bolometric detectors (possibly using radiation resistant detectors as in [6] to improve security). With such a long permissible response delay and the high performance of modern computer hardware, future routines for the ITER real-time tomography may become quite sophisticated. It should be noted that most of the present tomography routines would not be suitable since they rely on data from other diagnostics which are only available after the plasma discharge. Step-by-step development of the technique is therefore essential.

## 2. Rapid tomography and SXR position measurements on TCV

On TCV, minimum Fisher regularization (MFR) is successfully applied in th e tomographic reconstruction [7] of both SXR and bolometric data. The SXR diagnostics consist of ten pinhole cameras, see Fig. 1, each with linear arrays of 20 Centronix photodiodes and 47$\mu$m beryllium filter foil [8]. The MFR method is run on grid of rectangular pixels. The default size of a pixel is 37 mm, full coverage of the TCV cross-section corresponds to 15x42 pixels. The tomographic routine retrieves local emissivities in pixels $g_j$ so that they sum-up to projection data $f_i$:

$$f_i = \sum_j^P T_{ij} g_j \tag{1}$$

where P is total number of pixels and matrix $T_{ij}$ describes the set-up geometry. The inversion of these equations is underdetermined and ill-conditioned, forcing the introduction of additional constraints on the emissivity $g_j$. The principal constraint states that the emissivity profile be smooth, ie: there is some relation between pixel emissivity. Smoothing instructions depend on the reconstruction method. In MFR, the inversion matrix is determined by

$$M_{ji} = \left( \sum_l^L T_{jl} T_{li} + \lambda \sum_k^P B_{jk} w_k B_{kj} \right) \backslash T_{ji} \tag{2}$$

where L is total number of viewing lines and $B_{jk}$ correspond to first-order derivation imposed on the pixel grid. Smoothing coefficients, ie global regularisation parameter $\lambda$ and local weighting factors $w_k$, are found in two nested iteration loops so that the conditions on expected errors and minimum Fisher information are fulfilled [7]. The backslash matrix division $\mathbf{A\backslash C}$ stands for numerically advantageous transcription of $\mathbf{A}^{-1}\mathbf{C}$ .

In the rapid version of the MFR the smoothing coefficients are time averaged [4] so that a single inversion matrix $M_{ji}$ is sufficient for a whole sequence of experimental data:

$$g_{j\tau} = \sum_{i}^{L} M_{ji} f_{i\tau} \tag{3}$$

where $\tau$ indexes the time-slices. Next, plasma position in its time dependence $[r_\tau, z_\tau]$ is found as the centre of gravity of the SXR emissivity core evolution. The emissivity core $G_j$ is defined by $G_j = 0$ for $g_j < l$, $G_j = g_j - l$ for $l \leq g_j \leq L$ and $G_j = L - l$ for $g_j < L$. The lower limit $l$ and the upper limit $L$ are determined as a percentage of the maximum value of the instantaneous emissivity. Here from

$$[r_\tau, z_\tau] = \frac{\sum_j^P [r_j, z_j] G_{j\tau}}{\sum_j^P G_{j\tau}} \tag{4}$$

where $[r_j, z_j]$ is the position of the j-th pixel's centre. Notice that set of eqs. (3) together with (4) allow for very efficient numeric evaluation using a single-line matrix operation.

Tests runs with phantom emissivities validated our opinion that the position according to (4) is more reliable if a simplified version of inversion matrix (2) with no weighting ($w_k = 1$) is applied [4]. If we omit the iteration and pre-set the regression coefficient $\lambda$ according to the expected parameters of the experiment, the inversion matrix $M_{ji}$ may be pre-calculated and kept fixed for the inversion process. The algorithm for real-time tomography with position output then would reduce to single-time eq. (3), the core extraction and eq. (4). A brief feasibility study of the necessary processing hardware is presented in section 3.

Recently, rapid tomography was applied to all SXR data which are available in the TCV database and at time-slices corresponding to stored magnetic reconstruction data. In total, reliable SXR emissivities from 6325 TCV shots with a total of 332520 time-slices were calculated. The SXR centre of gravity $[r_{sxr}, z_{sxr}]$ according to (4) was then compared with the stored position of magnetic axis $[r_{mag}, z_{mag}]$. Distribution of position differences $r_{mag} - r_{sxr}$ and $z_{mag} - z_{sxr}$ is in Fig. 2. It demonstrates the resolution capabilities of the two position measurements and existence of systematic errors. As mentioned in the figure caption, the origin of most of the errors was discovered. Multiple linear regression was run on the position differences to unfold their dependencies on time, toroidal magnetic field, plasma position and plasma shape [4]. A clear increase in the disgreement with toroidal magnetic field was revealed which also accounts for an observed position shift during experiments with inversed toroidal field. Next, the time dependence of the differences was identified as

corresponding to minute plasma position drift during TCV shots. The effect can be seen in the plot of vertical differences in case of shots with long plateau phase, see Fig. 3. Interestingly, the drift even changes sign in the vertical direction from an average 2.4 mm/s downward to average 1.4 mm/s upward in 2001 while keeping to ~0.6 mm/s outward in radial direction. The slow global motion is most likely due to electronic drift in analogue integrators of TCV magnetic probe feedback signals. We are thus persuaded that a feedback to SXR tomography would improve plasma control at these low frequencies.

Clearly, some of the systematic shifts (like the radial offset and radial distribution deformation) can be attributed to the tomographic reconstruction and their different definition of position. These differences can, however, be compensated via correction coefficients from statistical analyses of experimental or phantom data. In conclusion, the resolution of both diagnostics is quite satisfactory with the regression remainders (i.e. compensated position differences) standard deviations 3.1 mm in vertical direction and 2.2 mm in radial direction.

## 3. Technical feasibility of the real time tomography hardware

Real-time SXR tomography with position feedback on TCV translates to digitising 200 analogue signals $f_i$ , multiplying them with a pre-calculated inversion matrix $M_{ji}$ (typically 630x200 real numbers), finding maximum of the resulting emissivity tomograms $g_j$ (630 numbers), extracting the core of emissivity $g_j$, determining its center of gravity $[r_{sxr}, z_{sxr}]$, possibly multiplying it by compensation factors and, if necessary, converting the calculated position to analogue signals. On TCV, the maximum permissible delay for all these operations is 10 ms. The real-time tomographic inversion would improve if data averaging over a few samples was implemented (e.g. 25 samples at 250kHz $\Rightarrow$ 0.1 ms). It would be also advantageous to store the resulting tomograms to allow for direct post-shot analysis, graphical output and other real-time applications. Contrary to pioneering real-time tomography [2] we aim at a standard, accessibly programmable hardware system.

Three technical options were considered: Field Programmable Gate Arrays (FPGA), Digital Signal Processors (DSP) and CPCI (compact PC local bus) with dedicated embedded Pentium processor. Though FPGA is the fastest option, its implementation would be complex for a large number of input channels. Futhermore, FPGAs do not directly include all features of high level programming languages. The gate arrays could be

very efficient in the *on-the-fly* signal averaging task. The DSP system could solve the real-time tomographic reconstruction provided it was highly parallelised ie: large amount of programming development. The CPCI-Pentium system would be the most economical and the most robust solution with the proviso that it is fast enough.

We ran the tomographic inversion in high level programming environment (MatLab6) on Pentium Athlon 2 GHz processor as a test of CPU execution times. The results were quite satisfactory: 1.5 ms for the matrix multiplication itself and 0.5 ms for the subsequent determination of the emissivity core and its centre of gravity. Assembler optimised numeric libraries could further improve the CPU time of matrix multiplication. Therefore, present day CPCI-Pentium systems fulfil our requirements for computation speed. No major obstacles were identified elsewhere, so that we believe that this approach is feasible on a modern CPCI machine with the necessary acquisition boards.

An example system would require seven 32 channel boards and two 16 bit analogue outputs. A digital output line could be driven at the same time via a dedicated ethernet connection. A dual processor solution is being considered, with one processor handling the data in the non-interruptible mode whilst the other performs the other tasks. As an indication of what is available in the present day market, in all solutions, the manufacturer is expected to supply the application program interface (API) for the data acquisition for programming in a higher level environment, or using assembler optimised functions from other sources.

## Acknowledgements:

The authors appreciate the professional support of Peter Milne from D-TACQ Solutions Ltd., http://www.d-tacq.com/ .

This work was partly supported by the Swiss National Science Foundation.

## References:

[1] L.C. Ingesson et al., Soft X-ray tomography during ELMs and impurity injection in JET, Nucl. Fusion 38 (1998) 1675-1694

[2] E. van der Goot, Software for the real time X-ray tomography system at JET, JET Report JET-P(91)28, July 1991

[3] H. Weisen et al, Overview of TCV results, Nucl. Fusion 41 (2001) 1459-1472

[4] J. Mlynar et al, Rapid tomographic inversion and matching of magnetic axis with soft X-ray measurements at the TCV tokamak, CRPP Report LRP 732/02, to appear

[5] ITER physics basis, ch.8, Plasma operation and control, Nuc. Fusion 39 (1999) 2577-2625

[6] A.Sushkov et al., TCV High Resolution X-ray Imaging Diagnostic, Proc. 29th EPS Conference on Plasma Phys. and Contr. Fusion, Montreux (2002) ECA Vol. 26B, P-4.118

[7] M. Anton et al., X-ray tomography on the TCV tokamak, Plasma Phys. Control. Fusion 38 (1996) 1849-1878

[8] M. Anton, M.J. Dutch and H. Weisen, Relative calibration of photodiodes in the soft X-ray spectral range, Rev. Sci. Instrum. 66 (1995) 3762-3769

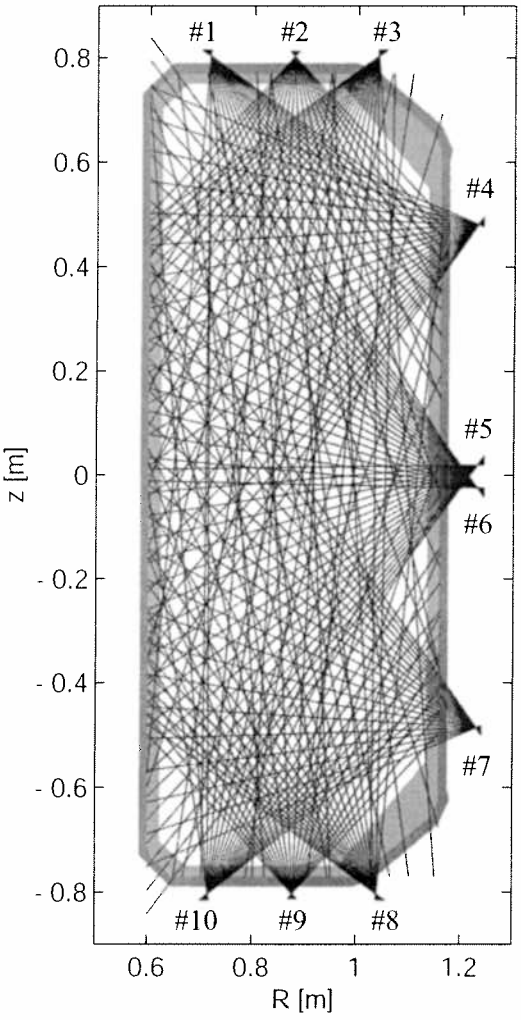


Fig. 1:
Setup of diagnostics for soft X-ray tomography shown in a TCV poloidal cross-section

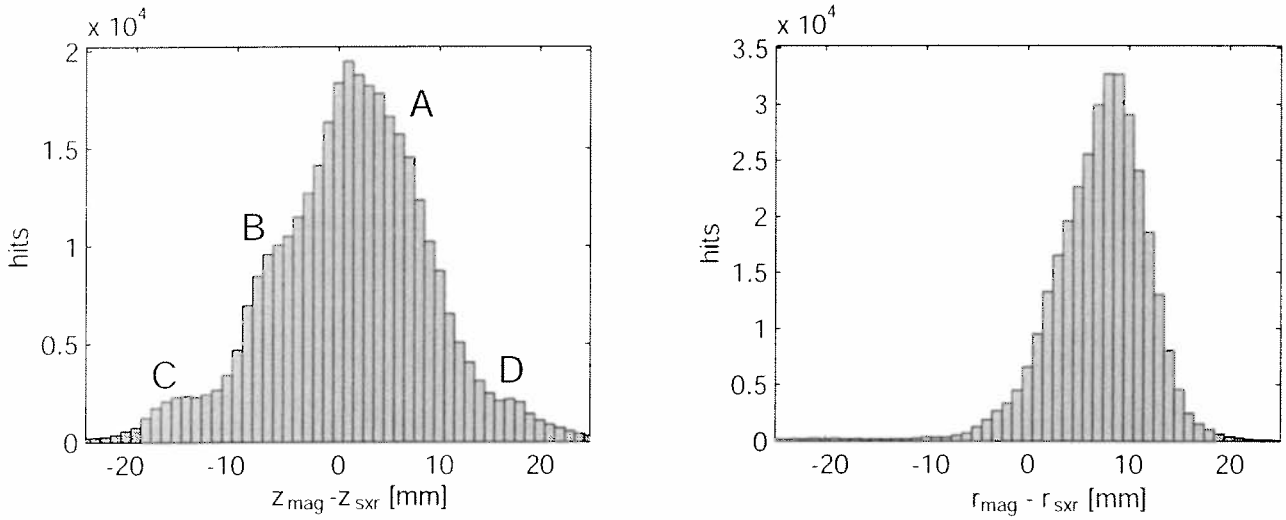


Fig. 2:
Differences in magnetic and SXR position measurements. Vertical direction (left):
A are mainly discharges before year 2001, B since 2001, C discharges with inversed magnetic field and D are mostly EC current driven discharges and some very early TCV discharges.
Radial direction (right): the displacement is a consequence of plasma D-shaping (i.e. the difference between the plasma centre of gravity and the plasma axis amplified by smoothing implicit in tomography) which is systematic and thus may be compensated [4]

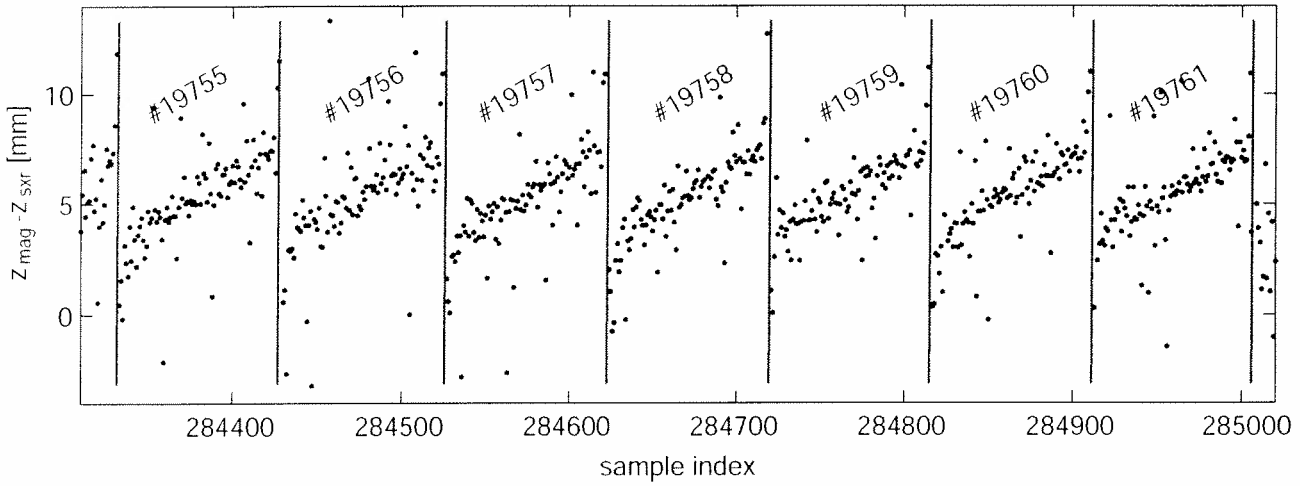


Fig. 3:
A series of long TCV discharges with constant zmag where the downward plasma drift is clearly visible. Individual discharges are separated by vertical lines.

# Analysis of the measurement of the current sharing temperature in the ITER TF Model Coil

C. Marinucci, L. Bottura*, P. Bruzzone

EPFL-CRPP, FT, CH-5232 Villigen PSI, Switzerland

* CERN, Div. LHC-MTA, CH-1211 Geneva 23, Switzerland

**Abstract**

The ITER Toroidal Field Model Coil has been tested in the TOSKA facility of FzK. The racetrack coil, which uses a circular Nb3Sn cable-in-conduit conductor, is equipped with external resistive heaters for the evaluation of the current sharing temperature (Tcs). Since there are no sensors inside the coil, the only possibility to assess the coil temperature is to use the measured inlet temperature and to estimate the downstream propagation of the temperature profile. The analysis has shown that a quantitative assessment of Tcs from the test results of the 60 s ramp heating run tends to overestimate the cable performance compared to the strand performance.

## 1. Introduction

The objective of the Toroidal Field Model Coil (TFMC) is to demonstrate the feasibility of superconducting coils wound in pancakes in a new type of winding designed for the full size ITER coils. The TFMC is a racetrack coil consisting of 10 pancakes nested in 5 radial plates (DP1-DP5), each with two joints at the inner and outer sides of the coil. The circular cable-in-conduit conductor uses Nb3Sn strands and a thin stainless steel jacket. The supercritical helium flows in the central cooling channel and the cable bundle, separated by a 1 mm thick stainless steel spiral. The TFMC is being tested in the TOSKA facility of the Forschungszentrum Karslruhe: in Phase I of the test program as a single coil (in 2001), in Phase II with the adjacent LCT coil (in 2002).

The heat generated by the heaters upstream of the inner joint (pancake DP1.1 and DP1.2) propagates through the joint and downstream to the high field region of the conductor. To heat the TFMC up to the current sharing temperature (Tcs), the ramp heating was proposed by CRPP as a compromise between two heating procedures: (a) the heat slug injection (the experiment has confirmed the result of early predictive analyses, i.e. the use of heating pulses is not viable due to helium choking [1]) and (b) the steady state heating (although expected to exceed the cryoplant capability, quasi steady state conditions could be reached in the experiment using multi step heating).

The analysis has focused on the run #72: single coil test, operating current Iop = 80 kA in the TFMC, ramp heating of 60s followed by a short plateau at constant power of 320 W in DP1.2 and 180 W in DP1.1, which ended with a quench.

## 2. Model

Conductor and joint hydraulic model (see Fig. 1) are described in [1]. Measurements have shown that the electrical resistance of the TFMC joints is in the range 1.6 - 1.7

nOhm [2]; we have assumed that the heat generated in half of the inner joint is 5.5 W, constant in time and uniformly distributed along the 50 cm joint length, and that the properties of the superconductor in the joint are the same as in the winding. Uniform current and uniform magnetic field in conductor/joint cross sections are assumed, using the average field modulus, i.e. disregarding the self field peak. The maximum field Bmax (~6.55 T) is located 1.2 m after the joint (X = 6.7 m, where X is the nodal coordinate along the conductor). The following parameters are retained to calculate the current sharing temperature (Tcs): the electrical field is 50 μV/m (the ITER design value for the TF coil), and the exponent of the power law index n is in the range 8 - 15 (the ITER design value is n = 10). The boundary conditions used for the analysis of DP1.2 are measured helium data, namely inlet temperature (TI712), outlet temperature (TI713), inlet pressure (PI702) and massflow rate. The pancakes DP1.1 and DP1.2 are assumed to be thermally insulated except at the inner joint where the heat exchange is a function of the temperature difference between them, whereas heat exchange and heat diffusion through the radial plates is not included in the model. The analysis is performed with the code Gandalf™ by CryoSoft.

## 3. Results and discussion

In the TFMC there are no sensors inside the coil; the only possibility to assess the temperature in the coil is then to use the measured inlet temperature (Tin) and to estimate the downstream propagation of the temperature profile. In the run with ramp heating, Tin is not a reliable figure to estimate the temperature in the coil because it overshoots at the end of the ramp. Our approach is then split into the following steps: (1) to use predictive simulations to assess the impact of the current sharing power on the local temperature; (2) to analyze the experimental run using the results of the simulations, and (3) to compare the above results with the expected Tcs resulting from scaling of the strand data.

### 3.1. Simulations

The simulations were mainly devoted to two objectives:

- to assess the time t50 at which an average electrical field of 50 μV/m develops in the coil, and the location of the initial normal zone;
- to assess the difference ΔT between the peak strand temperature at the selected resistive voltage criterion of 500 μV at quench and the maximum temperature at other V-criteria (e.g. 20, 50, 100 and 150 μV).

The time t50 and the temperature difference ΔT depend only on the ramp slope and the characteristics of the cable (index n). These being relative quantities, *ad hoc* parameters for longitudinal strain and heat exchange at the joint were inputted here to reproduce the experimental quench conditions.

The resistive voltage starts developing in the pancake DP1.2 at the time t = 76 s and peaks at tquench = 78.5 s when the runaway has started. The normal zone, i.e. the length of conductor in which the strand temperature exceeds the current sharing temperature at 50 μV/m, is 1.3 m long at quench. The average electrical field reaches 50 μV/m at t50 = 76.1 s. The normal zone at t50 is short (~15 cm) and occurs half a meter upstream from the location of Bmax (at X = 6.2 m where B = 5.88 T). These results

were obtained using n = 15. If n = 8 is retained, with the same resistive voltage at tquench the 50 μV/m electrical field develops 0.9 s earlier (t50 = 75.2 s).

The strand temperatures at quench detection and at t50 are affected by the current sharing power leading to the runaway. The difference ΔT decreases with increasing resistive voltage, being zero at 500 μV. At the criterion of 50 μV/m the resistive voltage is ~ 20 μV, the current sharing power in the short length exposed to Bmax is < 1.5 W and can be neglected. These results are for n = 15. With n = 8 the current sharing power increases by ~35% with respect to the results with n = 15.

### 3.2. Experiment

Goal of the analysis of the Experimental run #72 is to extrapolate, from the measured inlet temperature, the strand temperature at t50 and at the mid point location of the normal zone, assuming zero current sharing power.

Two different data acquisition systems were available for run #72: the slow DAS at 0.2 Hz sampling rate, and the fast DAS at 100 Hz. In the critical few seconds preceding the quench, the fast DAS is the only system capable to capture the realistic evolution of the input temperature. An adjacent averaging over 51 points is used to reduce the high noise level.

The analysis was performed using as a parameter the heat exchange across the joint, at the end of the ramp heating (QHXJ). Realistic values of QHXJ, extrapolated from CEA measurements in SULTAN, are in the range 30-40 W [3]. Using the input temperature of the fast DAS, the temperature T50 varies in the range from 9.67 K (index n = 15 and QHXJ = 30 W) to 9.36 K (n = 8 and 40 W) as shown in Fig. 2. The sensor accuracy is +/- 0.3 K. Using the inputs of the slow DAS, the corresponding range of T50 is 9.40 - 9.17 K. The variation of T50 with QHXJ is small (~ 15 mK/W) and linear in the range investigated.

### 3.3. Strand data and discussion

In Nb3Sn CICC with thin steel jacket the thermal longitudinal strain in the strand was measured in the range of -0.69% to -0.66% [4]. Including the operating strain at 80 kA, which is in the order of +0.1%, the total longitudinal strain (ε) retained for Nb3Sn is in the range -0.59% to -0.56%. The current sharing temperature is computed in the code Gandalf™ using Summer's law and the design value of the critical conductor parameters based on measured strand data [1]. At 80 kA and 6.44 T, the expected Tcs is 9.03 K at ε = -0.59% and 9.14 K at ε = -0.56% (Fig. 3).

The quantitative assessment of the Tcs from the test results of the 60 s ramp heating run tends to overestimate the cable performance compared to the strand performance, namely the difference is in the range of 0.64 - 0.22 K (fast DAS) and 0.37 - 0.03 K (slow DAS). A low index n in the CICC contributes to mitigate the above discrepancy. To explain this discrepancy, we suggest that more heat diffuses radially from the conductor into the rest of the coil, depressing the actual temperature at the quench location.

## 4. Conclusions

The analysis of the measurement of the current sharing temperature in the ITER Toroidal Field Model Coil (Experimental run # 72), has shown that:

- the ramp heating leads to a quench in the winding (and not in the joint) of the TFMC, as predicted by the analysis;
- a quantitative assessment of the Tcs from the test results of the 60 s ramp run ($dT/dt \sim 6$ K/min) tends to overestimate the cable performance compared to the strand performance, and this is likely due to heat diffusion from the heated conductor into the coil through the radial plates (not accounted in the analysis);
- as far as the cryoplant allows, a very slow ramp would be suitable to assess the conductor limits, avoiding the small transients of the multi step heating.

## 5. Acknowledgments

We would like to thank the FZK Team of P. Komarek for the kind hospitality and valuable discussions during the tests and the participants to the TFMC Test and Analysis Meetings for comments and information.

## 6. References

[1] C. Marinucci and G. Vécsey, Heat front propagation and quench initiation analysis of the ITER Toroidal Field Model Coil, Cryogenics, 40, 8-10 (2000), 501-510.

[2] D. Ciazynski et. al., Resistance of electrical joints in the TF Model Coil of ITER. Comparisons of first test results with sample results, 17th Int'al Conf. on Magnet Technology, 2001, to appear.

[3] P. Libeyre (editor), ITER Toroidal field model coil (TFMC). Test and Analysis Summary Report. Chapter 1: Specific analysis results needed for testing, CEA Report AIM/NTT-2001.005, June 2001.

[4] W. Specking et. al, First results of strain effects on critical current of incoloy jacketed Nb3Sn CICC's, Proc. of 15th Int'al Conf. on Magnet Technology, Science Press, Beijing, 1997, pp. 1210-1213.

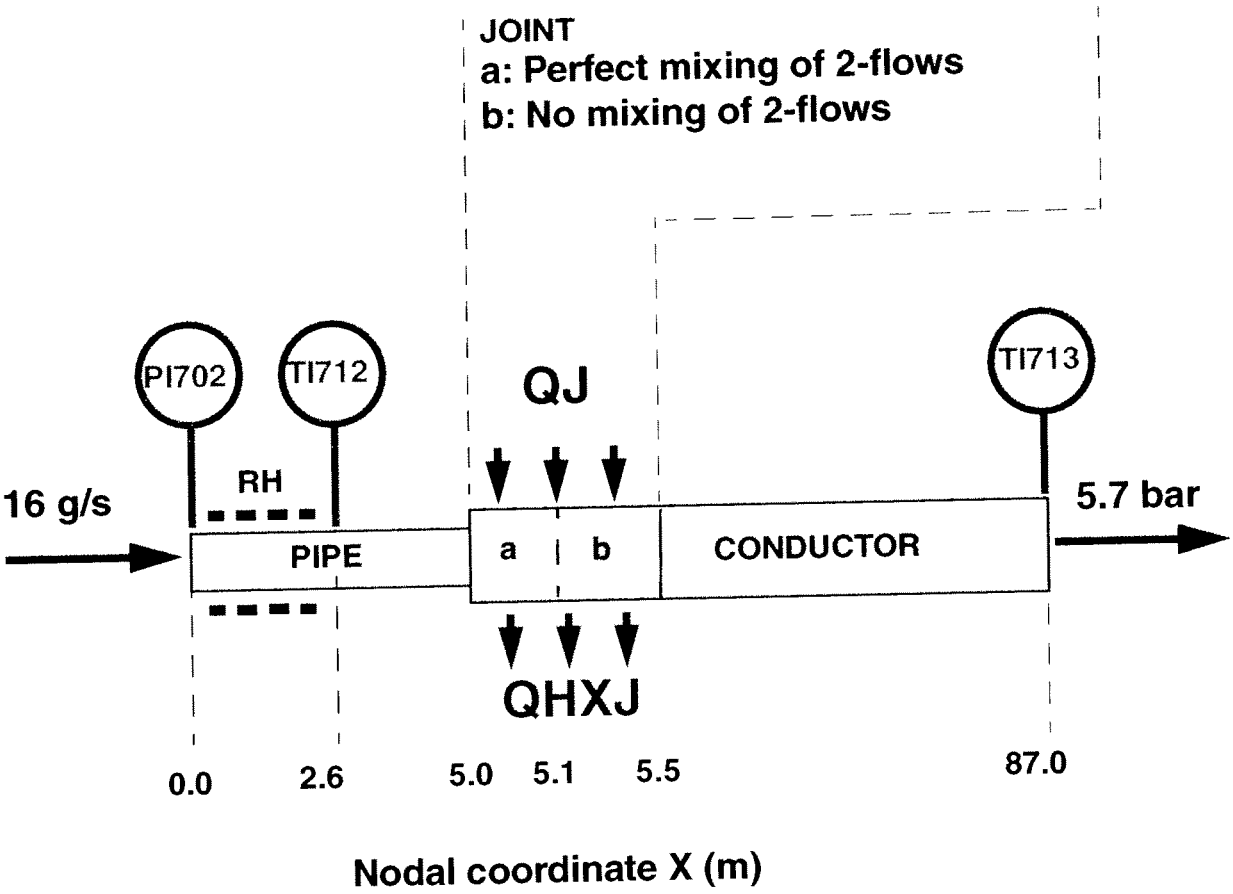


Figure 1. TFMC model (pancake DP1.2). The resistive heat (QJ) and the heat exchanged to the adjacent pancake DP1.1 (QHXJ) are uniformly distributed along the joint length. PI702, TI712 and TI713 are measured helium data used as boundary conditions. The outlet pressure is constant (5.7 bar) and tuned to match the experimental steady-state massflow (16 g/s). The resistive heater (RH) is not part of the simulation model.

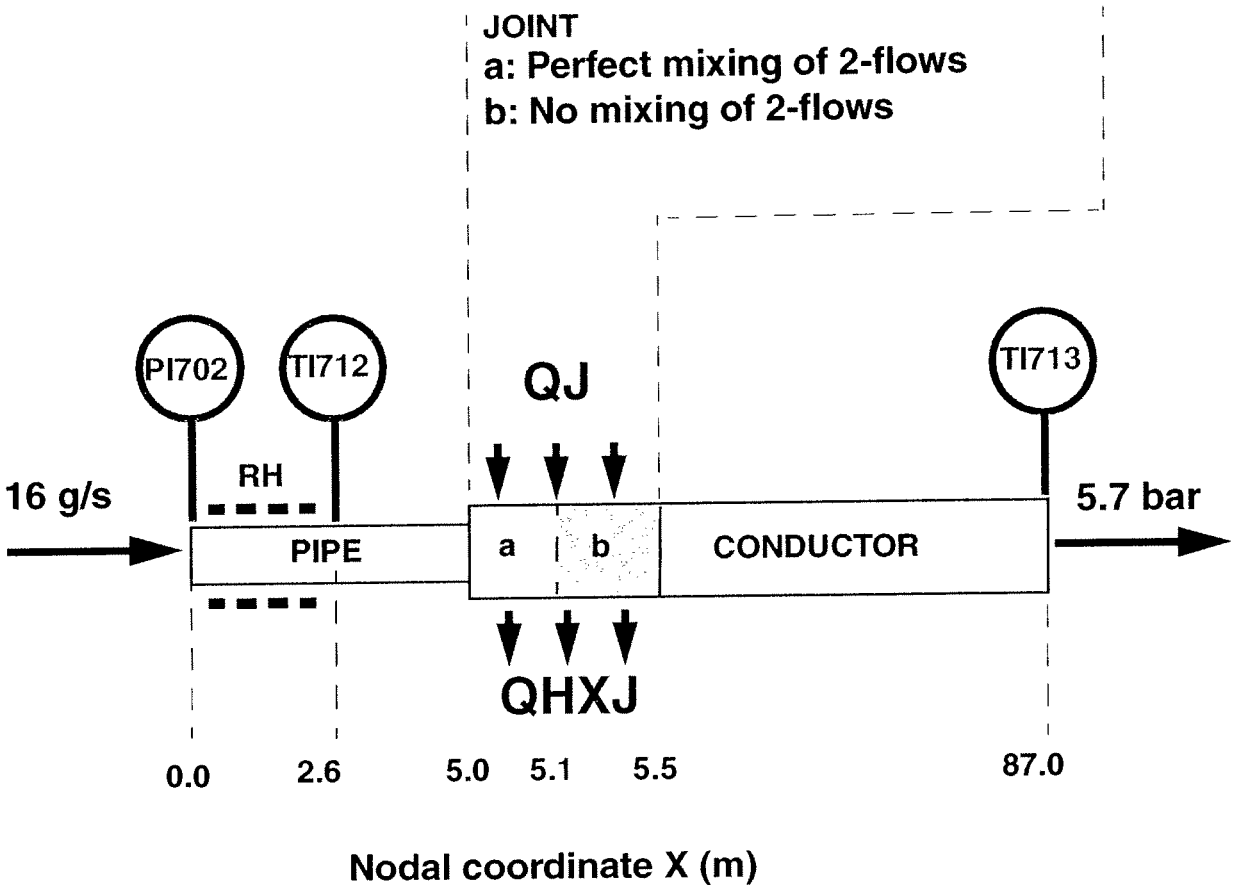


Figure 1. TFMC model (pancake DP1.2). The resistive heat (QJ) and the heat exchanged to the adjacent pancake DP1.1 (QHXJ) are uniformly distributed along the joint length. PI702, TI712 and TI713 are measured helium data used as boundary conditions. The outlet pressure is constant (5.7 bar) and tuned to match the experimental steady-state massflow (16 g/s). The resistive heater (RH) is not part of the simulation model.

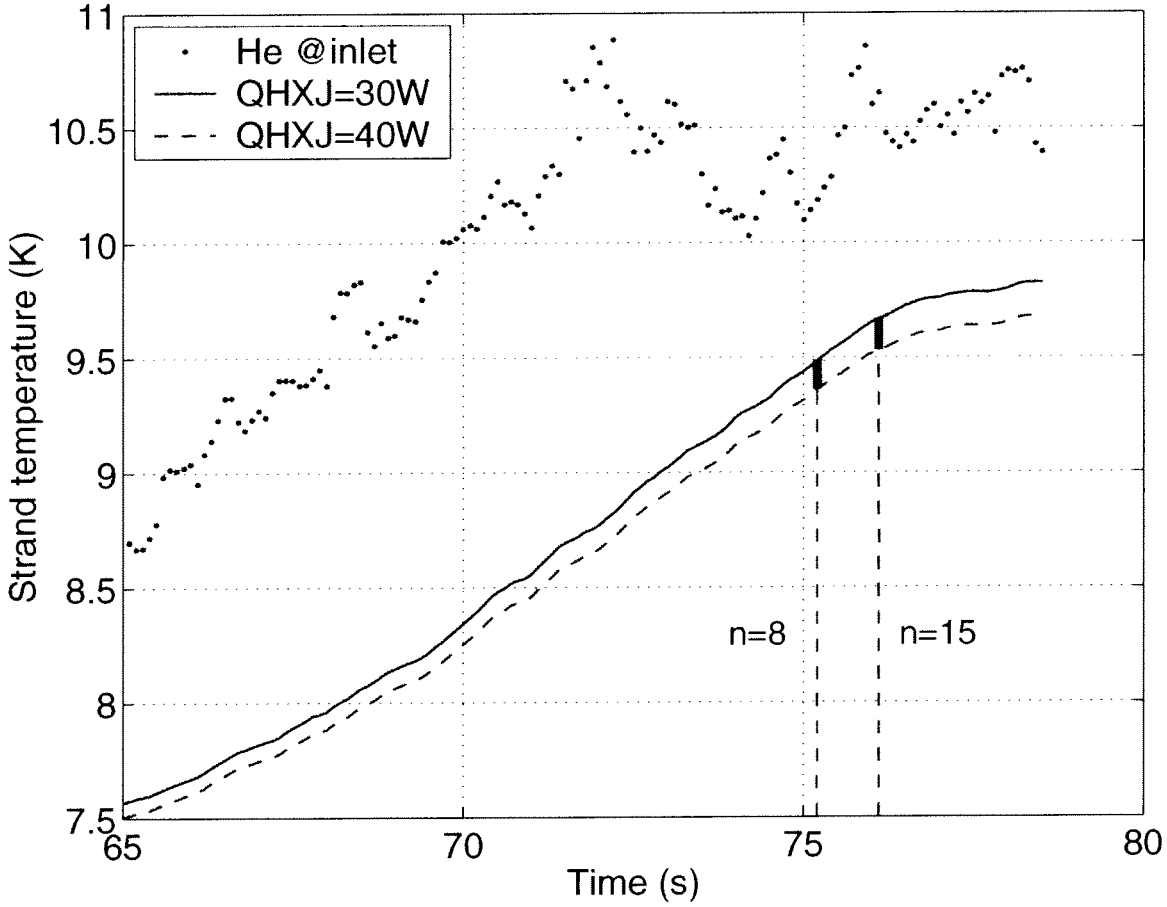


Figure 2. Experiment run #72 (fast DAS). Strand temperature at the assessed location of the quench for two values of the heat exchange at the joint QHXJ. The range of temperature variation with QHXJ, at the time when 50 $\mu$V/m are generated in the cable, is indicated for n=15 (76.1 s) and n=8 (75.2 s). The measured helium temperature at the inlet is also shown.

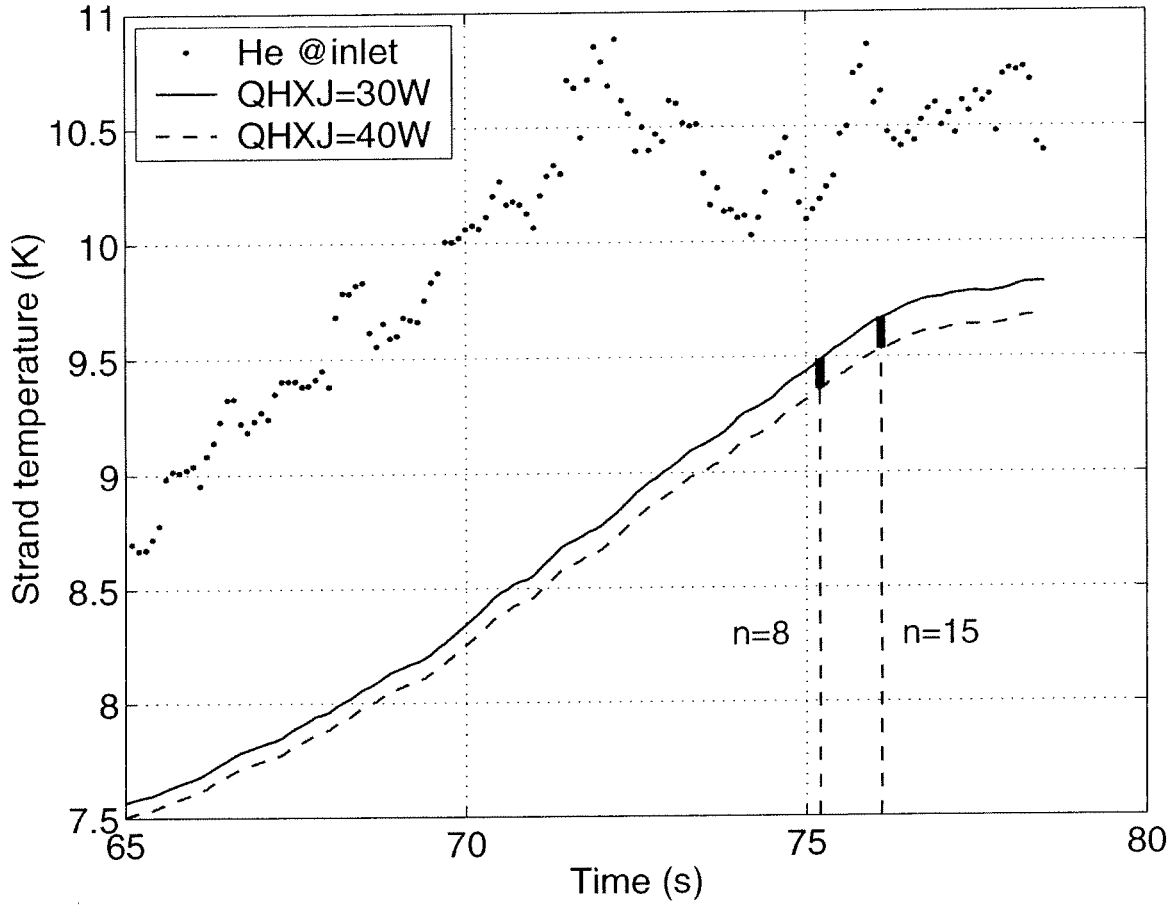


Figure 2. Experiment run #72 (fast DAS). Strand temperature at the assessed location of the quench for two values of the heat exchange at the joint QHXJ. The range of temperature variation with QHXJ, at the time when 50 μV/m are generated in the cable, is indicated for n=15 (76.1 s) and n=8 (75.2 s). The measured helium temperature at the inlet is also shown.

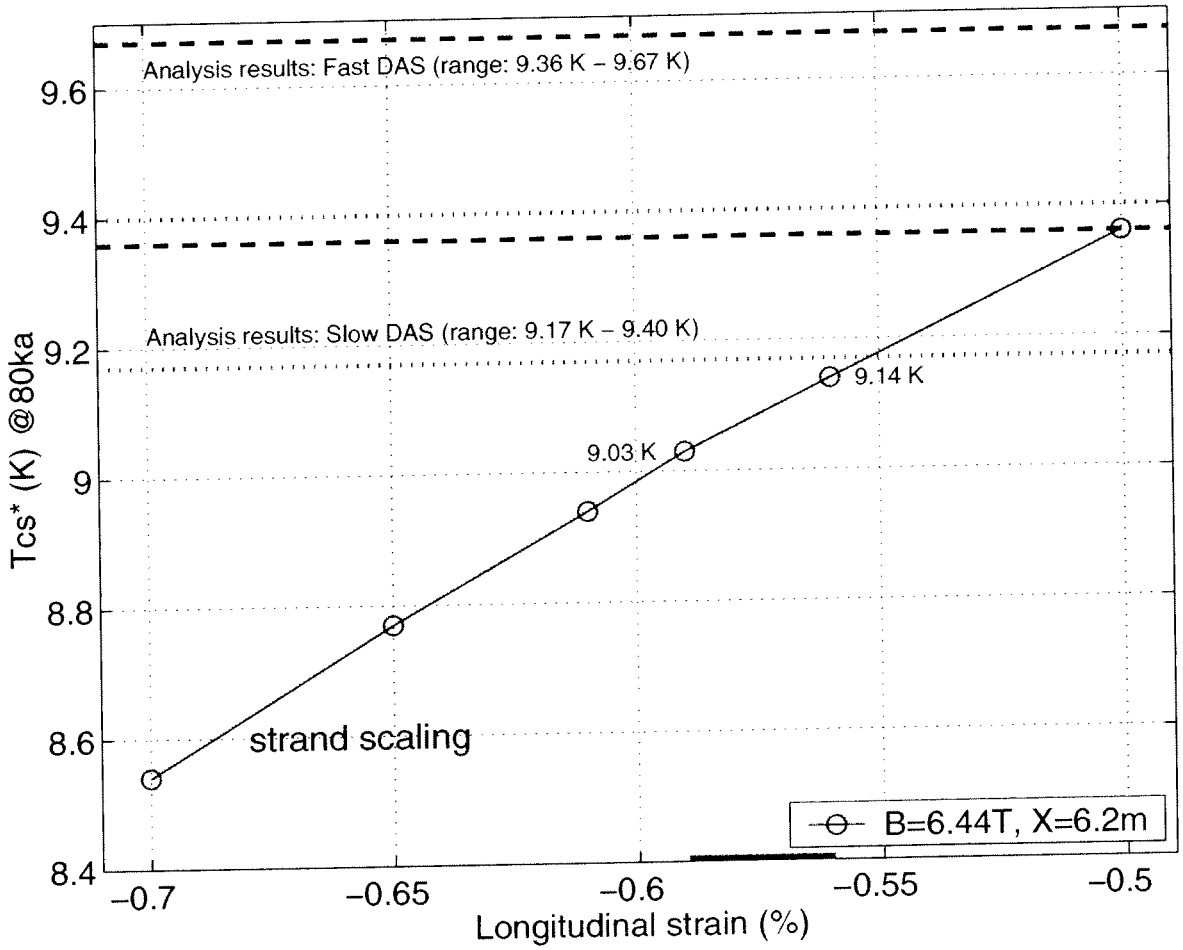


Figure 3. Current sharing temperature scaled from strand data as a function of the total longitudinal strain ε (at the middle line and for 80 kA) . The range of ε for the ITER TFMC is -0.59% to -0.56%, including the operational strain of +0.1%. The likely range of the temperature at t50 is also shown.

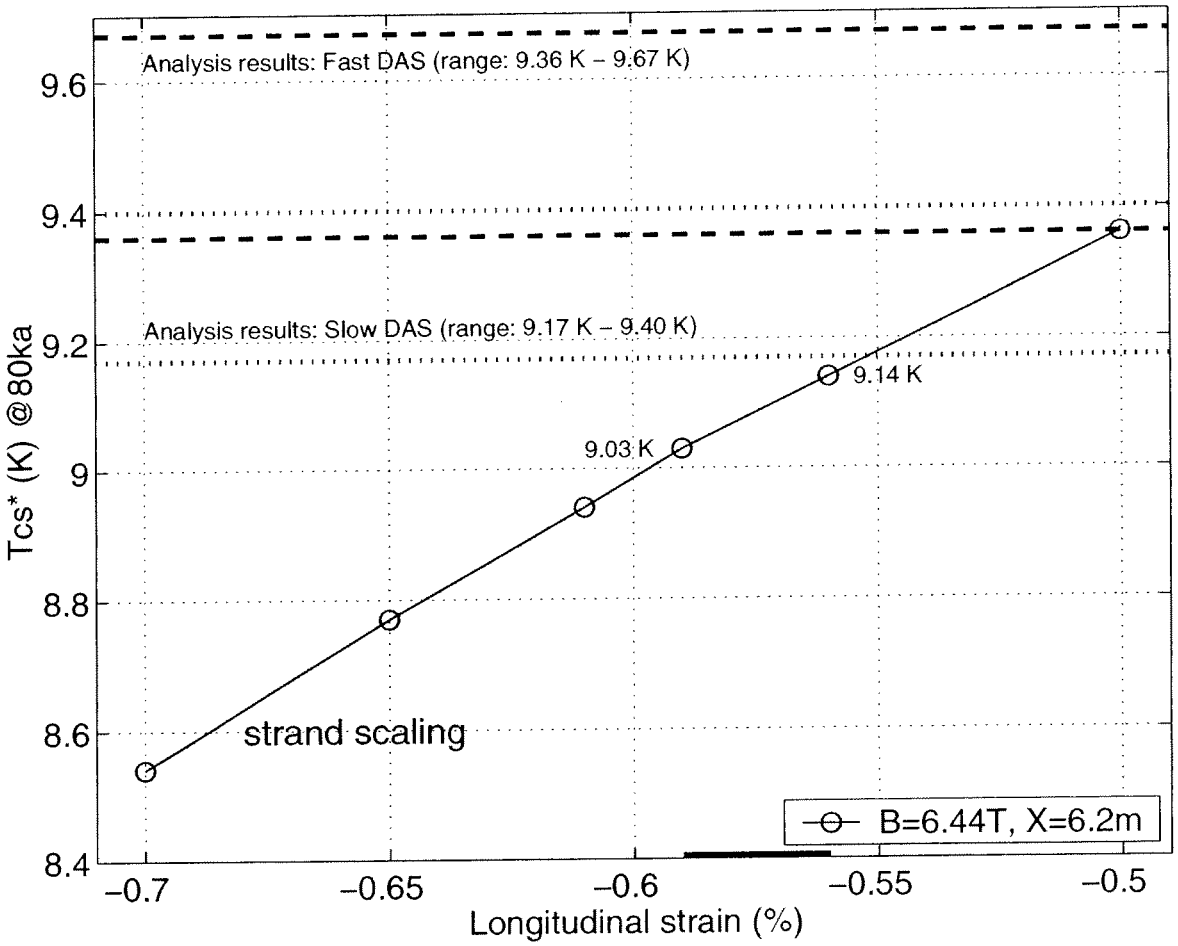


Figure 3. Current sharing temperature scaled from strand data as a function of the total longitudinal strain ε (at the middle line and for 80 kA) . The range of ε for the ITER TFMC is -0.59% to -0.56%, including the operational strain of +0.1%. The likely range of the temperature at t50 is also shown.

## DC Behaviour of NbTi Cable-in-Conduit Conductors for ITER-FEAT

R. Wesche, B. Stepanov, M. Vogel, T. Gloor, and P. Bruzzone

Centre de Recherches en Physique des Plasmas, CH-5232 Villigen PSI, Switzerland

**Abstract**

Using the SULTAN test facility the dc behaviour of 3 subsize NbTi cable-in-conduit (CIC) conductors has been studied. The dc performance of the cables is compared to the critical currents and the current sharing temperatures expected from the strand data. As a basis for this comparison the critical current of the NbTi strands has been measured in the temperature range of 4.2 to 6.5 K in magnetic fields of up to 7.5 T. The dc performance of the NbTi subsize conductors has been found to be not significantly affected by cyclic loading. In addition, the index of resistive transition of the cables is close to the values determined for the strands. Taking into consideration the self field of the conductor the cable critical current and the current sharing temperature are in agreement with the strand data.

Keywords: Cable-in-conduit superconductors, critical current, NbTi, self field effect

### 1. Introduction

The design of the poloidal field (PF) coils of ITER (International Thermonuclear Experimental Reactor) is based on the use of NbTi CIC superconductors. The design values of the operation current density of the NbTi conductors for the PF coils range from 190 to 980 A/mm$^2$ at 5 K and peak fields of 6 and 4 T, respectively. In the scope of a conductor optimisation program, 5 subsize NbTi CIC conductors have been designed and procured with parametric variations by CRPP. These hairpin short samples (2 × 3.5 m long) are presently tested in SULTAN [1] to study the relation between the conductor and the strand properties. In the present work, the results of the dc tests for 3 CIC conductors are compared, with either Ni or SnAg coated strands. The ac loss and the stability behaviour of the conductors is described elsewhere [2].

### 2. Experimental Details

The strand critical current was determined by the standard four-probe method using an 0.1 μV/cm criterion to define $I_c$. The $I_c$ values at temperatures between 4.5 and 6.5 K were measured in a temperature variable cryostat placed in the bore of a superconducting magnet [3]. The strand measurements were performed in the field range of 4 - 7.5 T. Because of the self-heating of the sample holder at high currents, the range of current is ≤400 A.

The main characteristics of the 3 hairpin NbTi subsize CIC conductors are listed in Table 1. The strands of NbTi 1 and 3 are coated with Ni, while the strands of NbTi 2 are coated with a SnAg solder. The cable layouts of NbTi 2 and 3 are identical. A special feature of NbTi 1 is a large number of segregated copper wires.

**Table 1.** Main design values of the investigated NbTi CIC subsize conductors.

| | NbTi 1 | NbTi 2 | NbTi 3 |
|---|---|---|---|
| **Strand diameter** | 0.87 mm | 0.70 mm | |
| **Cu : non-Cu** | ≈1.12 | ≈1.05 | |
| **Strand coating** | Ni | SnAg | Ni |
| **Cable pattern** | (1+7)×3×4×4 | (1+6)×3×4×4 | |
| **1. stage** | 1 NbTi strand + 7 Cu wires | 6 NbTi strands + 1 Cu core | |
| | $d_{Cu}$ = 0.62 mm | $d_{Cu}$ = 0.70 mm | |
| **Cable/Conduit diameter** | 16.5 mm/18.5 mm | 16.5 mm/18.5 mm | |

The $I_c$ of the subsize CIC conductors was measured in the field range of 5 - 8 T in SULTAN [1]. In each leg of the conductor a pair of voltage taps of 300 mm distance, placed in the high field region, is available for the measurement of the quench ($I_q$) and the critical current. In addition, the helium temperature in both legs of the conductors is measured before and after the high field region. To measure the quench ($T_q$) and the current sharing temperature ($T_{cs}$) the magnetic field and the current are kept constant, while the helium inlet temperature is continuously increased by means of a heater. The $I_c$ and $T_{cs}$ values are based on an 0.1 μV/cm criterion. Both types of measurements are performed at a helium mass flow rate of 2.5 g/s.

The dc tests for NbTi 2 and 3, distinguished only by the strand coating, are carried out before and after cyclic loading to study the effect of mechanical loads on the dc performance. The cyclic loading is performed by charging the conductor for 1400 times with a current of 40 kA in a field of 5 T. The resulting peak load $\sigma_p = BI/d_{cs}$, where $d_{cs}$ is the diameter of the cable space, reaches 12 MPa, which is well above the design value of 7 MPa for the PF coils of ITER.

## 3. Results and Discussion

### 3.1 Critical Currents of the NbTi Strands

The measured temperature and field dependencies of the $J_c$ of both NbTi strands can be well represented by the recently proposed scaling law [4]

$$J_c(B,T) = \left(\frac{C_0}{B}\right)\left(1-\left(\frac{T}{T_c}\right)^{1.7}\right)^{\gamma}\left(\frac{B}{B_{c2}(T)}\right)^{p}\left(1-\frac{B}{B_{c2}(T)}\right)^{q} \qquad (1)$$

where $T_c$ is the critical temperature and $B_{c2}(T) = B_{c20}(1-(T/T_c)^{1.7})$ the upper critical field. The differences of the fit parameters $C_0$, $B_{c20}$, $\gamma$, $p$ and $q$ obtained for the two NbTi strands used to fabricate the CIC subsize conductors are of the order of the error bars (see Table 2). For comparison, the fit parameters reported for another NbTi strand [5] are included in Table 2.

**Table 2.** Scaling parameters used to represent the temperature and field dependencies of the $J_c$ values of the NbTi strands. For comparison, the data for another NbTi strand of 0.81 mm diameter are included [5].

| | | | |
|---|---|---|---|
| $d$ (mm) | 0.87 | 0.70 | 0.81 |
| $p$ | 1.55 | 1.65 | 1.42 |
| $q$ | 1.85 | 1.80 | 1.63 |
| $\gamma$ | 1.79±0.08 | 1.88±0.04 | 2.11 |
| $B_{c20}$ (T) | 16.00±0.37 | 15.89±0.19 | 14.9 |
| $T_c$ (K) | 8.79±0.14 | 8.74±0.08 | 8.90 |
| $C_0$ (kA T/mm$^2$) | 285±12 | 272±5 | 248 |

### 3.2 Quench and Critical Currents of the NbTi Subsize Conductors

In Fig. 1, the $I_q$ values of NbTi 2 (SnAg coated) and 3 (Ni coated) are compared. The data shown in the figure have been obtained after 1400 load cycles. Especially at high current density, the $I_q$ values of NbTi 2 are up to 10 % higher than those of NbTi 3. The higher ac loss measured in the SnAg coated conductor [2] indicates that the effective transverse resistance of this conductor is by a factor of ≈5 smaller than in the Ni coated conductor. The quench is expected to occur first in the strands at the peak field. Due to the lower current sharing power, the thermal runaway is delayed and higher $I_q$ values are observed. The effect of a reversed current direction has been studied for the Ni coated conductor. The $I_q$ values are slightly enhanced for the reversed current direction, which may be a consequence of the reduced self field from the other leg. The effect of cyclic loading on the quench current of both conductors is negligible in spite of a ≈50 % higher effective transverse resistance in the solder coated conductor after cyclic loading. The results suggest that the current transfer among strands is not significantly affected by a moderate increase of the transverse resistance.

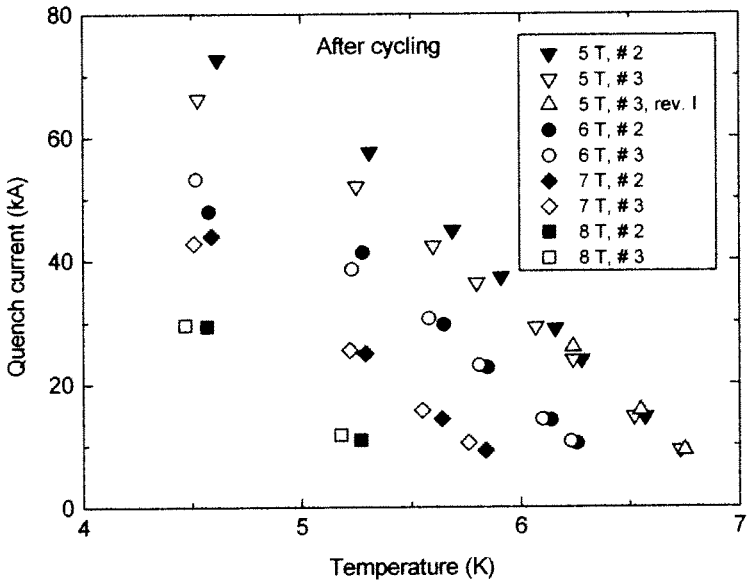


**Figure 1.** Quench currents of NbTi 2 and 3 after 1400 load cycles for various magnetic fields. The $I_q$ values of NbTi 3 are slightly enhanced for the reversed current direction.

The $I_c$ values of NbTi 2 and 3 after cyclic loading are shown in Fig. 2. The highest $I_c$ values measured at 5 T are ≈44 and ≈23 kA for NbTi 2 and 3, respectively. These values are much lower than the maximum $I_q$ values of ≈73 and ≈66 kA, which have been reached at the same field but at lower temperatures (see Fig. 1). Based on the strand data $I_c$ values above 70 kA can be expected at 5 T and 4.5 K even for the peak field. Consequently, NbTi 2 and 3 are unstable for operation at 5 T and $J$ values in excess of ≈810 and ≈430 A/mm$^2$, respectively.

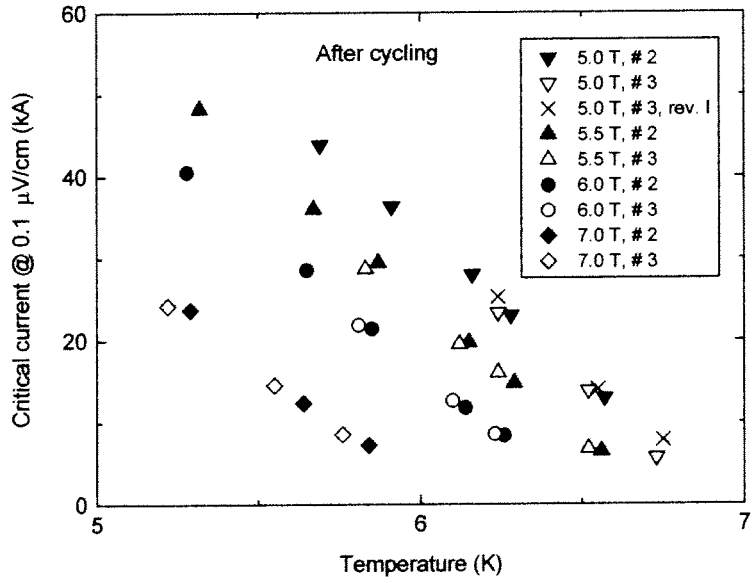


**Figure 2.** Critical currents of NbTi 2 and 3 after cyclic loading for various magnetic fields. The $I_c$ values of NbTi 3 are slightly enhanced for the reversed current direction.

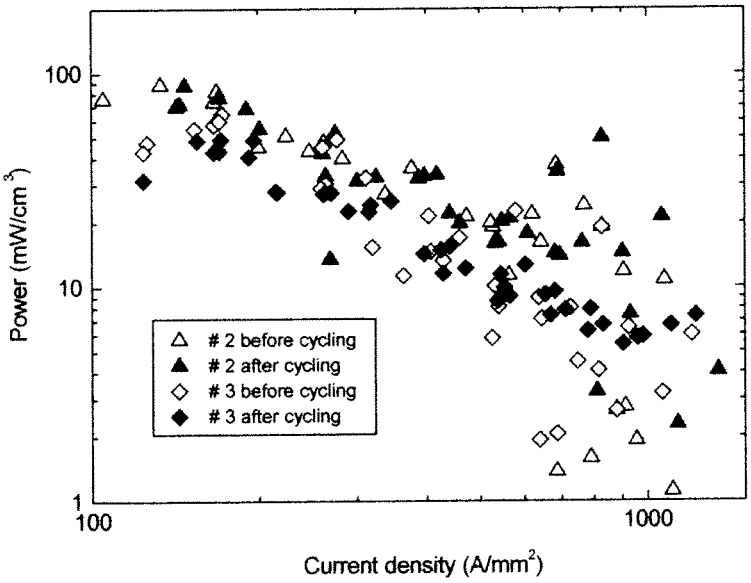


**Figure 3.** Power per unit volume generated at the quench in NbTi 2 and 3 versus current density. In spite of the enlarged scatter at high $J$ values the data suggest that the power required to initiate a quench is enhanced in both conductors after cyclic loading.

Due to the smaller transverse resistance the dc stability of NbTi 2 seems to be considerably better than that of NbTi 3. Nevertheless, an enhanced Cu : non-Cu ratio is required for both conductors for stable operation at low fields and $J \geq 1000$ A/mm$^2$. Similar to the quench currents the $I_c$ values are not significantly affected by the cyclic loading. The transient field stability of the two conductors has been found to be dominated by the ac loss behaviour. As a consequence of the lower ac loss, the transient stability of the Ni coated conductor is better than that of the SnAg coated conductor [2].

The take-off voltage has been found to decrease from $\approx$7 to $\leq$0.2 $\mu$V/cm when the current density increases from 100 to 1000 A/mm$^2$. The resulting power per unit volume of NbTi generated at the quench is shown in Fig. 3. The results suggest that the power required to quench the solder coated conductor is slightly higher than that necessary to quench the Ni coated conductor. This behaviour may reflect the different transverse resistance. However, for both conductors the quench power at high $J$ values seems to increase after cyclic loading in agreement with the fact that the $I_c$ could be measured up to lower temperatures in both conductors after cyclic loading. The improved stability after cyclic loading cannot be explained by the transverse resistance which is unchanged for NbTi 3, whereas it is even enhanced for NbTi 2. The enhanced quench power may be a consequence of reduced conductor movements after cyclic loading.

### 3.3 Quench and Current Sharing Temperature

The $T_q$ values of NbTi 1 - 3 before cyclic loading are compared in Fig. 4. Generally, the $T_q$ values for the Ni coated conductor NbTi 3 are lower than those of the SnAg coated conductor NbTi 2. This result is in agreement with the slightly lower $I_q$ values for NbTi 3 and may be a consequence of the higher transverse resistance. Interestingly, the $T_q$ values of NbTi 1, with a large amount of segregated copper, are considerably higher than those of NbTi 3. This behaviour seems to reflect the much lower self field contribution to the magnetic field for NbTi 1. The $T_{cs}$ values of NbTi 2 and 3 after cyclic loading are presented in Fig. 5 for currents between 8 and 20 kA corresponding to $J$ values between 150 and 370 A/mm$^2$. Typically the difference of the $T_{cs}$ values is less than 0.1 K.

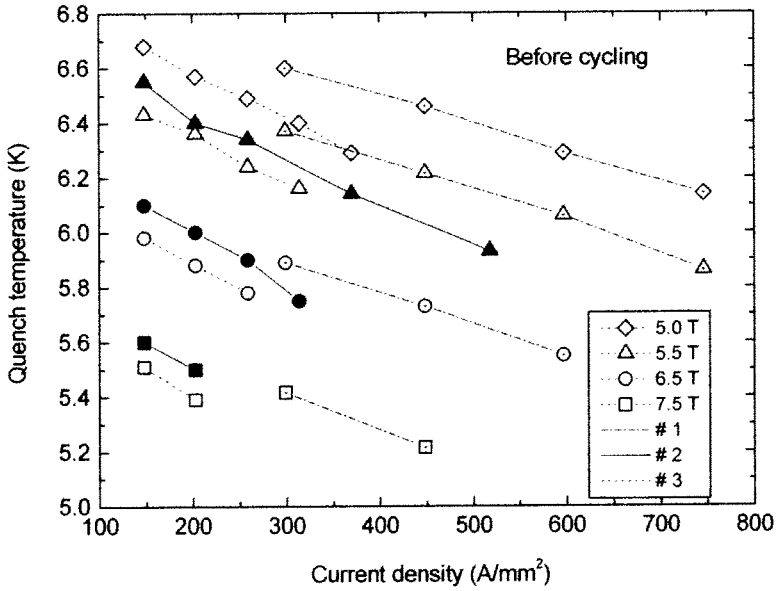


**Figure 4.** Comparison of the $T_q$ values of NbTi 1 (dot centred symbols), NbTi 2 (solid symbols) and NbTi 3 (open symbols).

3.4 Comparison of Conductor and Strand Properties

The $I_c$ values of NbTi 2 and 3 after cyclic loading are shown in Fig. 6 for different magnetic fields. The lines represent the $I_c$ values expected from the strand data for both the background and the peak field. For both conductors the $I_c$ values are close to the values calculated from the strand data for the peak field.

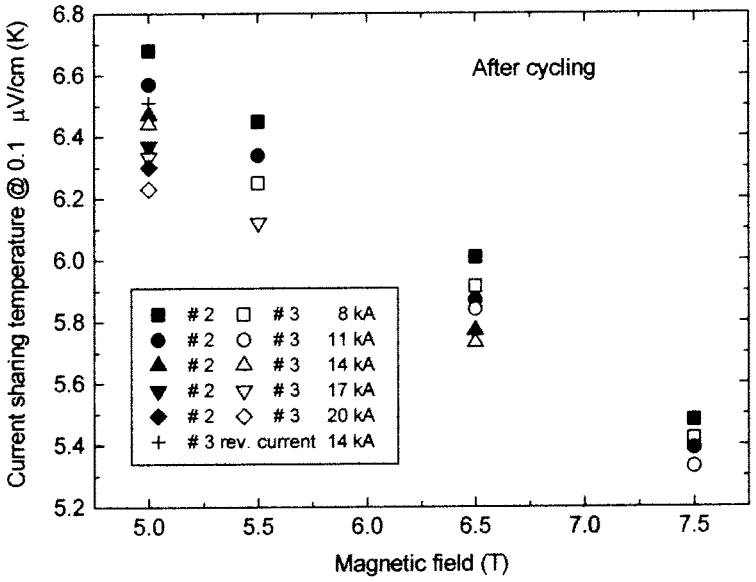


**Figure 5.** Current sharing temperatures of NbTi 2 and 3 versus magnetic field for 8 kA $\leq I \leq$ 20 kA corresponding to 150 A/mm$^2$ $\leq J \leq$ 370 A/mm$^2$.

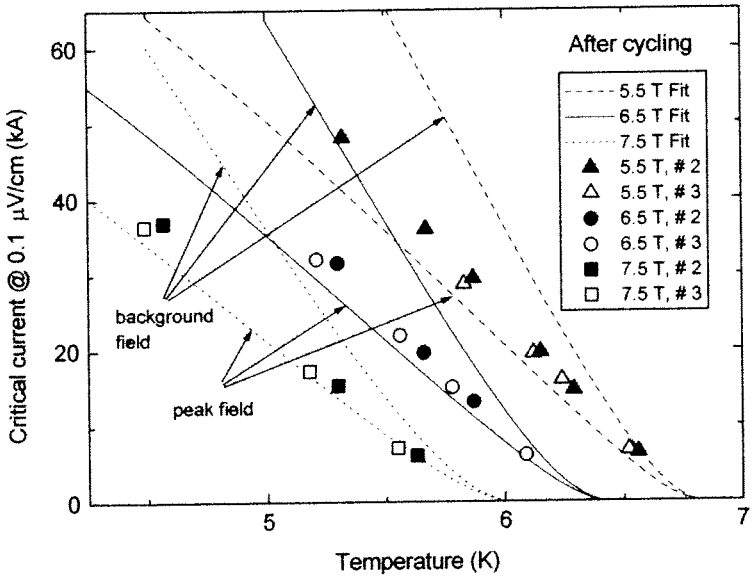


**Figure 6.** Comparison of the $I_c$ values measured for the CIC conductors NbTi 2 and 3 with the values expected from the strand data for both the background and the peak field.

The same behaviour has been observed for the $T_{cs}$ values of both conductors. Some of the $T_{cs}$ values are even below the current sharing temperatures expected for the peak field. In the $T_{cs}$ measurements the systematic error due to the fact that the local conductor temperature is slightly higher than the measured helium temperature may be of more importance than in the $I_c$ measurements.

The $n$ factor, defined by the relation $E \propto J^n$ ($E$ electric field), of the cable could be determined only for $J \leq 460$ A/mm$^2$ (stable range of operation). The results indicate that the $n$ factors of NbTi 2 and 3 are not significantly changed by cyclic loading. Considering the $n$ values as a function of the current density the $n$ values of both conductors are close to the strand data [6].

## 4. Conclusions

The data indicate that the $I_c$ values of the NbTi subsize CIC conductors are only slightly above the values expected from the strand data for the peak field. In the design of NbTi CIC conductors at least 2/3 of the peak field should be taken into consideration. The current carrying capacity of the conductors is not degraded by cyclic loading. Considering the same current density, the index of resistive transition $n$ of the cables is comparable to the strand data. To ensure stable operation of NbTi conductors for $J \geq 1000$ A/mm$^2$ a copper : non-copper ratio much larger than 1 is required.

## Acknowledgement

The authors are indebted to Felix Roth for technical assistance.

## References

[1] P. Bruzzone et al., Upgrade of operating range for SULTAN test facility, Proc. MT17, Geneva 2001, to appear.

[2] P. Bruzzone et. al, Parametric studies of subsize NbTi cable-in-conduit superconductors for ITER-FEAT, Proc. ASC, Houston 2002, to appear.

[3] R. Wesche, Temperature dependence of critical currents in superconducting Bi-2212/Ag wires, **Physica C 246** (1995) 186-194.

[4] L. Bottura, A practical fit for the critical surface of NbTi, **IEEE Trans. Appl. Supercond. 10** (2000) 1054-1057.

[5] Yu. Ilyin et al., Critical properties of EM NbTi strand for the PF conductor R&D, Intermediate Report, University of Twente, UT- EFDA 2001-4, May 2001.

[6] P. Bruzzone et al., The voltage/current characteristic (*n* index) of the cable-in-conduit conductors for fusion, Proc. ASC, Houston 2002, to appear.

# DINA simulations of TCV Electron Cyclotron Heating Discharges

V. E. Lukash[2], D. Raju[3], V. N. Dokouka[4], J-Y. Favez[1], R. R. Khayrutdinov[2] and J. B. Lister[1]

[1]Centre de Recherches en Physique des Plasmas,

Association EURATOM-Confédération Suisse, EPFL, 1015 Lausanne, Switzerland

[2]RRC Kurchatov Institute, Moscow, Russia

[3]Institute for Plasma Research, Bhat, Gandhinagar-382428, India

[4]TRINITI, Troitsk, Russia

## Abstract

This paper reports on full tokamak discharge simulations in the TCV tokamak using the DINA code, of which a new open modular architecture version is presented. These new simulations include the effect of intense electron cyclotron heating, dissipated off-axis. The change in the plasma conductivity produces a time-varying plasma current profile which in turn causes the plasma shape to relax in the almost constant vacuum quadrupole field. These simulations allow us to check on the diffusion of poloidal magnetic flux, as well as the modelling of the electron cyclotron heating.

## 1. Introduction and description of the DINA-SIMULINK model

Considerable effort has been dedicated on several tokamaks to benchmarking the DINA 1.5D axi-symmetric, time-dependent tokamak plasma simulation code [1]. Ohmically heated TCV plasma discharges have been successfully validated by DINA [2,3]. These results encouraged us to extend the simulation to a full discharge evolution of shaped TCV plasmas with electron cyclotron heating.

These simulations of TCV discharges using the DINA code are part of a remote collaboration between the TCV team and the DINA code developers from the RRC Kurchatov and TRINITI institutes in Moscow. The first results mentioned were generated in simulations in which the plasma equilibrium response was the part of most interest and in which the precise implementation of the TCV control system model was somewhat less significant. Some minor discrepancies between the modelling and the experiment were difficult to trace and a collaborative effort was undertaken to translate the DINA simulations, totally implemented in Fortran, into the Matlab-Simulink environment [4]. Matlab-Simulink offers transparent access to the tokamak simulation parameters and to the simulation results and is ideally suited to plasma control simulations due to a vast library of intrinsic functions available. The full simulation set up can be viewed graphically with seamless transfer of the simulation data to direct visualisation of the results.

In order to achieve this, all details of the particular tokamak device were removed from the DINA simulations and re-implemented as external Matlab-Simulink building blocks. The reduced DINA code, independent of the device, was then implemented as a so-called

S-function [4] which is simply a linkable module which can be graphically implemented as a Matlab-Simulink building block. This is illustrated schematically in Fig. 1.

The motivation for this is to provide a generic axi-symmetric tokamak DINA module which, hopefully, would require minimum modifications and maintenance during the exploitation of the code. The physics remaining inside the code includes the electromagnetic circuit evolution, the evolving plasma equilibrium, the transport of poloidal flux, particles and heat, the electron-ion equilibration power, neo-classical resistivity (including impurities) and radiated power.

An initialisation routine generates the tokamak-specific data, including the geometry and electrical properties of both the active Poloidal Field coils and passive axi-symmetric current-carrying structures. It prepares an initialisation of the simulation including the equilibrium parameters, the control system parameters and the feed-forward and feedback reference waveforms ,which are needed to simulate the full TCV PF control system.

We shall see in the discussion that this implementation was successful. DINA is tending towards a validated, efficient mathematical tool for solving the equilibrium and transport equations for a generic tokamak. At present, the transport physics is defined internally, although converting the heat transport to an open modular architecture would seem a natural next step. We refer to this version of DINA as "DINA-Simulink", of which a more primitive version had originally been developed in collaboration with the DIII-D team.

The first attempts at simulating a full discharge will inevitably give unsatisfactory results. Any difference in the plasma inductance leads to a constant offset between the simulated and experimental primary transformer currents during the plasma current flat-top. Any

difference in the plasma resistance leads to a roughly linear divergence between the same. Trying to tweak a time-dependent plasma resistance, either ad hoc or by tweaking the plasma transport is time-wasting and pointless, since it teaches us nothing. In [2] we removed any offset or constant drift from the measured and simulated PF currents, with full justification. In the full pulse DINA simulations we have chosen a more pragmatic approach. A low gain feedback loop is added to the DINA simulations allowing the divergences of the primary transformer currents to be corrected by adjusting a linear plasma resistance multiplier, a "$Z_{eff}$ modifier", onto neo-classical resistivity.

Several other factors such as transport coefficients, width and location of heat deposition, location of an internal transport barrier, density profile must be adjusted properly to obtain a simulation reasonably close to the experiment. What is "reasonable" depends on the question which the simulation is trying to answer.

## 2. Implementation of the TCV ECH system

The TCV ECH system has both record power and record power density at present. Its flexibility allows heating and current drive at any minor radius compatible with propagation of the EC wave within the plasma, limited to relatively low densities when the waves are launched at the second harmonic (82.7 GHz) from the outboard side of the plasma. In the present work, we excluded discharges with any current drive component. The target we set was to accurately reproduce TCV off-axis heating experiments previously reported [5]. In these discharges, the plasma shape is not under feedback control. When the off-axis heating is applied, the change to the conductivity profile leads to an evolution towards a broader steady-state current distribution and therefore leads to a change in the plasma elongation in

the almost constant quadrupole component of the vacuum poloidal field, as previously reported [5].

The poloidal angle of the ECH beams can be varied during the pulse and the power deposition varies in time, due to both the plasma shape and/or position variation and the beam launching geometry. Normal analysis of these discharges relies on the TORAY code, which calculates the beam trajectory and absorption for a cold plasma in (R,Z) geometry on the basis of the reconstructed equilibrium, and yields the power deposition in terms of the normalised radius. Using this deposition profile in the simulation would be dishonest, since a very different plasma position in the simulation would still have the experimentally correct deposition in terms of the normalised radius. However, calculating the beam deposition in real-time using TORAY during the simulation would be extremely time-consuming. The compromise chosen is to convert the TORAY results back into (R,Z) geometry and impose the centroid and width of the power deposition on the simulation. This is still not completely self-consistent, since a different plasma shape would still lead to different diffraction of the EC beam, and therefore a different (R,Z) deposition from that calculated from the measured plasma profiles in TORAY. We consider this as a secondary effect, until proof to the contrary. The input to the DINA simulation is therefore the (R,Z) of the centre of the beam absorption, the width in the same rectangular co-ordinates and the instantaneous power, all imposed with a 1 msec time resolution.

### 3. Comparison of the simulations

We present simulations of TCV discharge # 19692, which is an ECH assisted discharge with far off-axis deposition. The results are shown in Fig. 2 and we examine the signals in

turn. The plasma current is well simulated, since it is fed back in closed loop in both the experiment and the simulation - the close agreement is inevitable. With the modification described above, the comparison of the simulated and measured OH transformer current is reasonable, although work is perhaps needed to improve on the quality of the agreement.

The vertical position of the magnetic axis is well modelled, again inevitable since this parameter is also under feedback control. The evolution of $\kappa_{95}$, the elongation of the equilibrium at the 95% poloidal flux surface, shows 3 curves, the experiment (dotted line) and two simulation results. In the first simulation, the electron heat conductivity (nominal T-11 scaling) is multiplied by two (grey line) and in the second one, it is multiplied by one (black line). We see a significant difference in the speed of the evolution of the plasma elongation when the conductivity is changed, whereas both simulations tend towards the same elongation. This result shows that DINA is correctly modelling this evolving equilibrium current profile, but that there is a large sensitivity to the evolution of the temperature profile, through variations in the assumed transport. The triangularity $\delta_{95}$, equilibrium parameters ($\beta$, li) and $q_{95}$ show good agreement. The evolution of the electron and ion temperatures shows, as expected, significant dependence on the assumed heat transport multiplier, but the simulations are comparable with the experimental values.

There are some other sources of disagreement possible in the DINA simulations. Differences between DINA and LIUQE results for plasma parameters can be due to the different set of equilibrium parameterisation used by these codes. In the case of the LIUQE inverse equilibrium code, reconstruction of the plasma evolution is done by means of a set of parameterised functions for plasma current and pressure profiles and a fitting algorithm

calculates the most suitable plasma parameters. However in DINA, the simulation starts with a set of initial conditions and then the plasma profiles evolve in a totally free manner.

## 4. Discussion

These preliminary but successful simulations show that the DINA model is capable of simulating the evolving equilibria produced by intense off-axis ECH power in TCV. The open modular architecture version DINA-Simulink provides a flexible platform for performing such simulations. Constraining the simulation to reproduce the measured transformer primary currents, corresponding to the experimental poloidal magnetic flux consumption, has provided a suitably pragmatic solution to time-consuming iterations to produce a good simulation. A similar approach to modifying the heat transport multiplier will be tested. Future work using DINA-Simulink will include simulating intense ECH with a significant current drive component.

**Acknowledgement**: The collaboration of the whole TCV team is recognised in this work which was partly supported by the Fonds National Suisse de la Recherche Scientifique.

**References:**

[1] R.R. Khayrutdinov and V.E. Lukash, J. Comp. Physics, **109** (1993) 193

[2] R.R. Khayrutdinov, J.B. Lister, V.E. Lukash and J.P. Wainwright, Plasma Physics and Controlled Fusion, **43** (2001) 321

[3] J-Y. Favez, R. R. Khayrutdinov, J. B. Lister and V. E. Lukash, Plasma Physics and Controlled Fusion, **44** (2002) 171

[4] Matlab - a commercial software product from Mathworks Inc.

[5] A. Pochelon et al., Nuclear Fusion **41** (2001) 1663

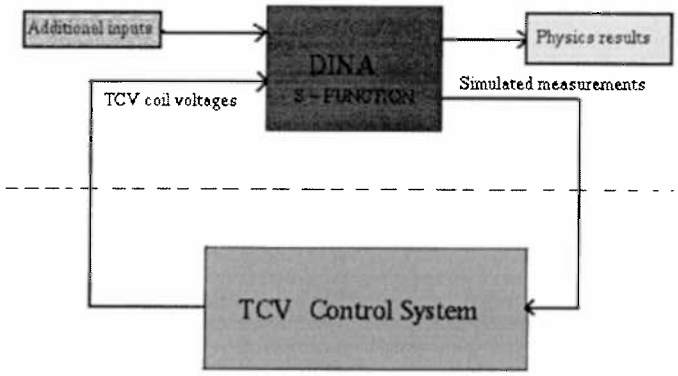


*Figure 1: TCV simulations with the DINA-Simulink model.*

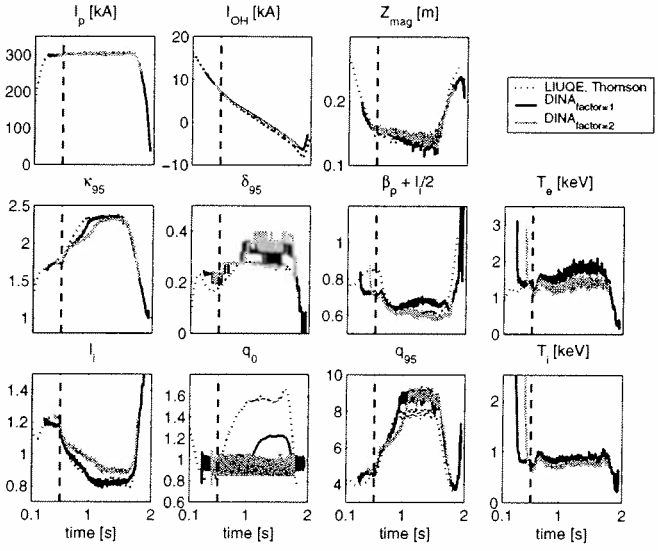


*Figure 2: Results of ECH assisted TCV discharge #19692 with two different simulations with electron heat conductivity multiplied by two (grey line) and multiplied by one (black line) compared with the experimental measurements (dotted line). The vertical dashed line indicates the ECH turn on time.*